

## The environmental dependence of mid-IR luminous dusty Supernovae

LIN XIAO <sup>1,2,3,\*</sup> ZEYUE PENG <sup>1,2,3</sup> LLUÍS GALBANY <sup>4,5</sup> TAMÁS SZALAI <sup>6</sup> ORI D. FOX <sup>7</sup> LEI HU <sup>8</sup>  
MAOKAI HU <sup>9</sup> THALLIS PESSI <sup>10</sup> YI YANG (杨轶) <sup>11,12</sup> TAKASHI J. MORIYA <sup>13,14,15</sup> ZHANWEN HAN <sup>16,17,18</sup>  
XIAOFENG WANG <sup>11,19</sup> AND SHENGYU YAN <sup>11</sup>

<sup>1</sup>Department of Physics, Hebei University, Baoding, 071002, China

<sup>2</sup>Hebei Key Laboratory of High-precision Computation and Application of Quantum Field Theory, Baoding, 071002, China

<sup>3</sup>Hebei Research Center of the Basic Discipline for Computational Physics, Baoding, 071002, China

<sup>4</sup>Institute of Space Sciences (ICE, CSIC), Campus UAB, Carrer de Can Magrans, s/n, E-08193 Barcelona, Spain

<sup>5</sup>Institut d'Estudis Espacials de Catalunya (IEEC), E-08034 Barcelona, Spain

<sup>6</sup>Department of Experimental Physics, Institute of Physics, University of Szeged, H-6720 Szeged, Dóm tér 9, Hungary

<sup>7</sup>Space Telescope Science Institute, 3700 San Martin Drive, Baltimore, MD 21218, USA

<sup>8</sup>McWilliams Center for Cosmology, Department of Physics, Carnegie Mellon University, 5000 Forbes Ave, Pittsburgh, 15213, PA, USA

<sup>9</sup>Physics Department, Tsinghua University, Beijing 100084, China

<sup>10</sup>European Southern Observatory, Alonso de Córdova 3107, Vitacura, Casilla 19001, Santiago, Chile

<sup>11</sup>Physics Department and Tsinghua Center for Astrophysics (THCA), Tsinghua University, Beijing, 100084, China

<sup>12</sup>Department of Astronomy, University of California, Berkeley, CA 94720-3411, USA

<sup>13</sup>National Astronomical Observatory of Japan, National Institutes of Natural Sciences, 2-21-1 Osawa, Mitaka, Tokyo 181-8588, Japan

<sup>14</sup>Graduate Institute for Advanced Studies, SOKENDAI, 2-21-1 Osawa, Mitaka, Tokyo 181-8588, Japan

<sup>15</sup>School of Physics and Astronomy, Monash University, Clayton, Victoria 3800, Australia

<sup>16</sup>Yunnan Observatories, Chinese Academy of Sciences, Kunming 650216, China

<sup>17</sup>Key Laboratory for the Structure and Evolution of Celestial Objects, Yunnan Observatories, CAS, Kunming 650216, China

<sup>18</sup>International Centre of Supernovae, Yunnan Key Laboratory, Kunming, 650216, China

<sup>19</sup>Beijing Planetarium, Beijing Academy of Science and Technology, Beijing, 100044, China

### ABSTRACT

Using the *Spitzer* and *WISE* images, we discovered 42 mid-IR luminous dusty supernovae with local integral-field spectroscopy data. The observed mid-IR emission indicates the presence of newly formed dust, or pre-existing dust heated by the radiation from the supernovae or circumstellar medium interactions. We carried out a systematic analysis of the supernova host environments and their dust properties, for understanding the dust-veiled exploding stars, and whether such an intense dust production process is associated with their local environments. We find that dusty supernovae prefer the locations with higher  $EW(H\alpha)$ , lower metallicity, and heavier host extinctions compared to typical SN types, and they show the same increasing sequence in the values of  $EW(H\alpha)$  and oxygen abundance from hydrogen-rich, type II<sub>n</sub> and hydrogen-poor dusty supernovae. These differences in environmental properties of different dusty SN types indicate the diversity of their progenitors. We also found that one marginal correlation is a negative correlation between the SN dust mass and star formation rate. This means that SNe would be more mid-IR luminous and more dust-rich at the region with lower star formation rate. However, the SN dust mass show no correlation with the metallicity and the host extinction, which were thought to be key factors affecting the mass-loss history of progenitors and the CSM environment of SNe. Therefore, the dust formation process in SNe might be insensitive to metallicity and the dust condition of their host environments.

*Keywords:* supernovae:general — infrared — circumstellar matter — galaxies:abundances

### 1. INTRODUCTION

The mid infrared (mid-IR) capability offered by the *Spitzer Space Telescope* (*Spitzer* hereafter), systematic searches of dust in supernovae (SNe) have been carried out over the past decade (see, Szalai et al. 2019, 2021

\* corresponding author: linxiao@hbu.edu.cn

for reviews). Spitzer Infrared Intensive Transients Survey (SPIRITS), provided a systematic mid-IR study of SNe of various types within nearby galaxies (Tinyanont et al. 2016; Kasliwal et al. 2017). Most of the dust emission in SNe can be attributed to being either pre-existing or newly formed dust heated by later-time circumstellar medium (CSM) interactions (Fox et al. 2011; Szalai & Vinkó 2013). The inferred dust mass is critical to determine whether SN is playing a major role in enriching the dust budget within the interstellar medium (ISM). The dust grain species and the radial distribution profile would provide an immediate trace of the progenitor’s pre-explosion mass-loss history, thus constraining the progenitor system (Matsuura et al. 2009; Fox et al. 2011, 2013; Fransson et al. 2014; Tinyanont et al. 2019).

Characterizations of the dust present in such dusty SNe have revealed the presence of a substantial amount of dust over a broad range of SN subtypes. Type IIn SNe were the original class of SNe exhibiting clear signatures of interaction with the surrounding CSM. Progressively, signs of SN interactions were found in more “normal” SNe and dust emission became dominated at late-time ( $> 100$ days) photometry. Meikle et al. (2011); Szalai et al. (2011); Andrews et al. (2016); Tinyanont et al. (2016) found a mid-IR rebrightening due to warm dust emission in type IIP SNe, which were also theoretically thought to be the best candidates for dust formation among SNe due to its thicker outer envelope (Kozasa et al. 2009; Gall et al. 2011). Some stripped-envelope SNe (including type Ib/c, Ibn, and I Ib) also show mid-IR emission at late times. The well-known case is SN 2014C which transformed from type Ib to an interacting type IIn over the course of a year (Milisavljevic et al. 2015; Margutti et al. 2017), and there is a strong and long-lasting interaction observed over thousands of days post explosion by *Spitzer* (Tinyanont et al. 2019). Such a transformation from a H-poor SN Ib/c to a H-rich interacting SN IIn had also been observed in SN 2001em (Chugai & Chevalier 2006) and SN 2004dk (Mauerhan et al. 2018). Additionally, Type Ia including its subtypes exploding in dense, H-rich CSM shells, can also be mid-IR bright with significant dust component (Silverman et al. 2013; Fox et al. 2015; Graham et al. 2017). A sub-luminous thermonuclear Type Iax SN 2014dt showed an excess of mid-IR emission at about one year post explosion (Fox et al. 2016), and a later ( $> +310$  days) rebrightening in mid-IR was observed in the type Ia-CSM SN 2018evt (Wang et al. 2024). Siebert et al. (2024) found a strong thermal dust emission was present in the “super-Chandrasekhar” mass type Ia SN 2022pul, suggesting for a SN exploding within CSM.

The ability of strong CSM interaction and significant dust production enables dusty SNe to heavily influence their immediate environments and the evolution of their host galaxies. The study of the SN environments, although not a direct approach, has been able to provide independent constraints on the properties of SN progenitor systems (Anderson et al. 2015; Chen et al. 2017; Galbany et al. 2018; Kuncarayakti et al. 2018; Xiao et al. 2019). Many SN environment analyses have used the capabilities of integral-field spectroscopy (IFS) to investigate the SN associated HII regions within host galaxies for a more precise study of the SN host environment. Recently, Pessi et al. (2023a) using data from the Very Large Telescope (VLT) with the Multi Unit Spectroscopic Explorer (MUSE) instrument studied 112 CC-SNe, and they found that stripped-envelope SNe (Ib and Ic) are located in environments with a higher median SFR and oxygen abundance than Type II. Based on the SN environmental study, Pessi et al. (2023b) investigate the dependence of CCSNe production on metallicity, and conclude that there is a strong decrease in the number of CCSNe per unit of star-formation as oxygen abundance increases. Xi et al. (2025) also studied the effect of metallicity in evolution of massive stars and their final core-collapse supernova (CCSN) explosions, but they found that metallicity plays a minor role in the origin of different CCSN types. (Moriya et al. 2023) studied the correlation of SN optical properties with their host environments in a sample of 21 Type IIn SNe, and they find that type IIn SNe with a higher peak luminosity are preferentially located in environments with lower metallicity and younger stellar populations.

A systematic characterization of dusty SN environments in different SN types could be of critical importance to understand the properties of the dust-veiled exploding stars, and whether SN dust formation is associated with the local environment of the progenitor populations. This is the main motivation of this first environment study of dusty SNe in the current work. This paper is organized as follows: Section 2 describes the selection of our dusty SNe, their mid-IR photometry of *Spitzer* and *WISE*, and the dust SED fittings. Section 3 makes a statistical analysis of the environmental properties of dusty SNe. Section 4 investigates possible correlation between SN dust and their environmental properties. Finally, we conclude this paper in Section 5.

## 2. OBSERVATIONS AND DATA ANALYSIS

### 2.1. Collection of Supernova Data from the IFS sample

We collected a sample of 275 nearby core-collapse supernovae (CCSNe) with IFS of their host galaxies from Galbany et al. (2018) (hereafter G18), Pessi et al. (2023a) (hereafter P23) and Moriya et al. (2023) (hereafter M23). This sample consists of 154 hydrogen-rich SNe (including IIP, IIL, II), 83 hydrogen-poor SNe (including IIB, Ib, Ic), and 38 type IIn SNe.

We note that our sample was taken from different works using different facilities. Firstly, G18 sample is constructed using 232 observed galaxies with IFS data from the PMAS/PPak Integral field Supernova hosts COmpilation (PISCO; Galbany et al. 2018), which is updated in terms of different SN subtypes including SN Ia and increased in the completeness of SN host galaxy sample with low-mass ( $< 10^{10}M_{\odot}$ ) galaxies. So the host galaxies have  $M_r$  varied from -24 to -12 mag and redshift up to 0.09 with median  $\sim 0.017$ . Due to the spatial pixel (spaxel) size of PISCO at  $1'' \times 1''$  (namely 1 arcsec<sup>2</sup> in area), a typical size of the HII region segregation in PISCO data can be a few hundreds of parsecs depending on distance (Galbany et al. 2018). This size is significantly larger than individual HII regions, and usually 1 to 6 HII regions were selected in data with that resolution (Mast et al. 2014).

Then for P23 sample, they are selected from the SN catalogue of All-Sky Automated Survey for Supernovae (ASAS-SN) and then covered by the All-weather MUse Supernova Integral field Nearby Galaxies (AMUSING) survey (Galbany et al. 2016b). Their host galaxies have redshift up to 0.06 with median  $\sim 0.011$  and  $M_B$  ranging from -23 to -16 mag. For AMUSING data, the spaxel size is  $0.2'' \times 0.2''$ , five times smaller than PISCO, which can zoom into SN parent stellar population better and decrease the contamination from nearby ones. M23 sample selected only type IIn host galaxies from the PISCO, AMUSING, and the Mapping Nearby Galaxies at APO (MaNGA; Bundy et al. 2015) surveys. The spaxel size of MaNGA is  $0.5'' \times 0.5''$ , in the middle of that of PISCO and AMUSING. As a whole, the HII region segmentation under the resolution of the three samples is larger than the physical scale of a real HII region, and the contamination from nearby stellar populations would affect our result using it as a SN parent stellar population.

Our IFS sample is a collection of these three samples, which show a spread distribution in host galaxy magnitude and redshift, and provide an unbiased analysis of different types of SN environments. Table 1 reports the local environmental properties of the dusty SNe we studied in this work. We measured the EW(H $\alpha$ ) which

can be a good measurement of the stellar population age of SN host HII regions, the star formation rate intensity  $\log\Sigma_{\text{SFR}}$  to trace the relation between star forming and SN explosion, the metallicity indicated by the oxygen abundance  $12+\log(\text{O}/\text{H})_{\text{D16}}$  measured by Dopita et al. (2016), and the E(B-V) of the SN host HII regions from the Balmer decrement given by Domínguez et al. (2013) to recognize any significant effect of extinction caused by ambient CSM or ISM, respectively. A more detailed description of the calculation of the SN local environmental properties can be found in Galbany et al. (2018).

### 2.2. Mid-IR photometry from Spitzer and WISE

The ‘dusty SNe’ we studied are mid-IR luminous SNe especially at late time ( $> 100$  days). Szalai et al. (2019, 2021) obtained the largest data set for over 100 SNe discovered to have late-time mid-IR emission. We cross-matched this *Spitzer* sample with the above PISCO/AMUSING/MaNGA SNe local environment sample and found only two SNe which are type IIP SNe SN 2003gd and SN 2013ej with identified dust measured.

The Wide-field Infrared Survey Explorer (*WISE*; Wright et al. 2010) has mapped and kept going on monitoring the entire sky at mid-IR wavelengths of  $3.4 \mu\text{m}$  (W1 band) and  $4.6 \mu\text{m}$  (W2 band) every half year since its launch in 2010 except the operational gap between 2011 and 2013. Compared to *Spitzer*, *WISE* is inferior in spatial resolution with 6.1 and 6.6 arcsec in the W1 and W2 bands respectively, but superior in the sample size and monitoring duration (Sun et al. 2022; Myers et al. 2024; Wang et al. 2024). Therefore, we expect that more SNe in the above IFS sample could be observed by *WISE*. We performed a photometric analysis of the CCSNe in the above IFS sample using the time-resolved unWISE<sup>1</sup> coadded images produced by Lang (2014); Meisner et al. (2017a,b). For each SNe, we created a reference image in each band by combining the pre-explosion images using SWarp (Bertin 2010). For all the post-explosion images, we performed image subtraction with SFFT (Hu et al. 2022) to eliminate the flux contamination from the galaxy background. Then aperture photometry is performed on the subtracted images using Photutils (Bradley et al. 2023). We used the standard aperture radius of 3 pixels and background annulus for the uncertainties from 18 to 25 pixels with 1 pixel of 2.75 arcsec following the explanatory supple-

<sup>1</sup> <https://irsa.ipac.caltech.edu/data/WISE/unWISE/overview.html>

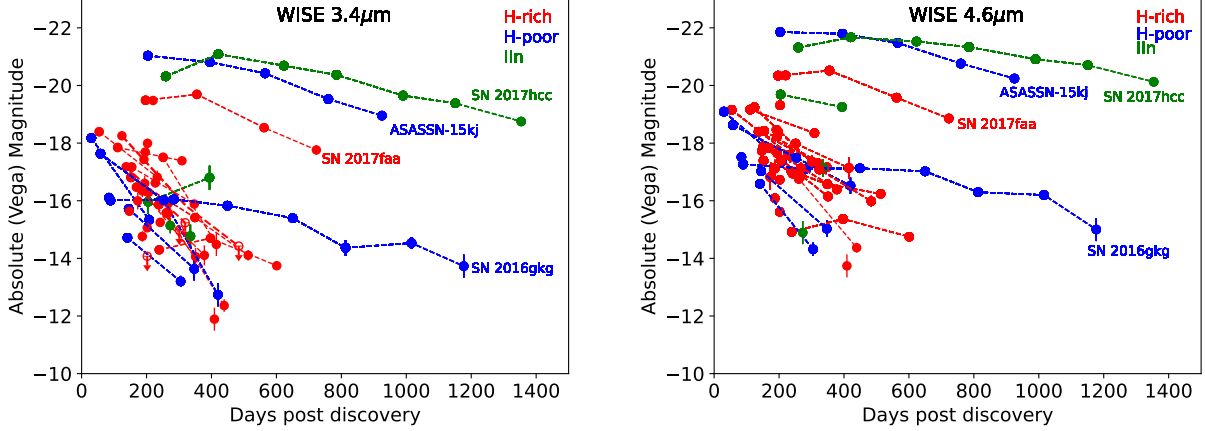


**Figure 1.** The mid-IR photometry of all detected SNe at the band of  $3.4 \mu\text{m}$  (left) and  $4.6 \mu\text{m}$  (right), except that SN 2003gd and SN 2013ej detected by *Spitzer* are at  $3.6 \mu\text{m}$  (right) and  $4.5 \mu\text{m}$  (left). The colors are for different subclasses with hydrogen-rich SNe in red, hydrogen-poor SNe in blue and type IIn SNe in green. In the left panel, the empty symbols with downward arrows denote SNe whose absolute magnitudes were calculated with a  $3\sigma$  upper limits. All data are listed in Table 3.

ment<sup>2</sup> of *WISE* data, and applied aperture corrections of 1.227 and 1.294 for  $3.4 \mu\text{m}$  (W1 band) and  $4.6 \mu\text{m}$  (W2 band), respectively. We set a  $3\sigma$  threshold for a positive detection in at least one *WISE* band. This  $3\sigma$  threshold in infrared SN studies was used by Fox et al. (2011) for *Spitzer* mid-IR photometry and has been widely adopted in works reviewed by Szalai et al. (2019). For *WISE* photometry, the same  $3\sigma$  criterion was also employed by Sun et al. (2022) and Wang et al. (2024). Finally, mid-IR emission was detected from 40 CCSNe, including 30 hydrogen-rich (H-rich) SNe, 7 hydrogen-poor (H-poor) SNe, and 3 type IIn SNe. We noted that there are four SNe (SN 2014ay, SN 2017gmr, SN 2018bb1, SN 2018cuf), which at some epochs are only positively detected at  $4.6 \mu\text{m}$ , and we calculated a  $3\sigma$  upper limit at  $3.4 \mu\text{m}$ . As discussed by Gutiérrez et al. (2020), SN2017ivv has a lower hydrogen mass than a typical SN II but more than a SN IIB, we included it in the group of H-poor SNe and labeled with II/IIB in Table 1.

Figure 1 plots the mid-IR photometry of all SNe with positive mid-IR detections including the two SNe detected by *Spitzer*. We note that the most SNe across all subtypes are detectable only within the first two years post discovery. These events are bright in mid-IR during the early-time CSM interaction, but the brightness declines quickly. We also highlight four specific targets: type II SN 2017faa, type Ic SNe ASASSN-15kj, type IIB SN 2016gkg, and type IIn SN 2017hpc, which produces a slowly declining mid-IR light curve in both  $3.4 \mu\text{m}$  and  $4.6 \mu\text{m}$  bands over two years and even up to 1000

days post discovery. Among the four SNe, Type IIn SN 2017hpc and type Ic SN ASASSN-15kj are extremely bright in mid-IR. For type IIn SNe, Fox et al. (2011, 2013) showed that the mid-IR radiation is more likely from pre-existing dust which is radiatively heated by optical emission generated by ongoing interaction between the SN forward shock and CSM. Type IIB SN 2016gkg, like SN 2001em and SN 2014C detected by *Spitzer* previously, seems to encounter a strong interaction with CSM at later times although this case is quite rare in H-poor SNe (Chugai & Chevalier 2006; Tinyanont et al. 2016). SN 2017faa is the third luminous one which is relatively brighter than other hydrogen-rich SNe, while SN 2016gkg is much dimmer than other longer-lived SNe. The diversity in mid-IR evolution of CCSNe likely corresponds to the extent of pre-SN mass loss that constructed their surrounding CSM, but may also suggest different shock velocities, progenitors and explosion environment.

So far the highest redshift of CCSNe detected by *WISE* is a type II SN 2018hov of  $z = 0.067$  (Myers et al. 2024). Given the detection limit of *WISE* in terms of redshift  $< 0.07$ , Figure 13 in appendix presents the redshift distribution of the IFS sample with the median redshift  $\sim 0.015$  ( $0.015 \pm 0.008$  in average), and only one type IIn SN 2017ghw of  $z = 0.0762$  in sample M23 lies beyond 0.07 which could be lost by the detection of *WISE*. In addition, we note that *WISE* observation scans the explosions since 2010 and have the most effective detection within the two years post SNe as shown in Figure 1, so that around 50% of CCSNe in the IFS sample occurred before 2008 could be dusty and mid-IR luminous but lost by *WISE*. Therefore, the SNe without positive detection by *Spitzer* and *WISE* could not be

<sup>2</sup> <https://irsa.ipac.caltech.edu/data/WISE/docs/release/All-Sky/expsup/index.html>

simply taken as non-dusty SNe. In this work, we would not discuss non-dusty SNe, and compared the mid-IR luminous dusty SNe detected by *Spitzer* and *WISE* with the whole IFS CCSN sample in terms of their environmental properties and in different typical SN types (H-rich, H-poor and type II<sub>n</sub>) as discussed in Section 3.

### 2.3. SED Fitting and Dust properties

Mid-IR ( $3 \leq \lambda \leq 25 \mu\text{m}$ ) SEDs of SNe span the peak of thermal emission of dust with temperatures in the range of  $100 \lesssim T_{\text{dust}} \lesssim 1000$  K, providing useful constraints on the properties of dust (Fox et al. 2011; Szalai & Vinkó 2013). We analyze the SNe following the method used in a number of papers (Fox et al. 2010, 2011; Szalai & Vinkó 2013; Tinyanont et al. 2016; Shahbandeh et al. 2023) by assuming thermal emission only from an optically thin dust shell, whose spectrum is expressed as:

$$F_{\lambda}^{\text{obs}} = \frac{M_{\text{dust}}^{\text{obs}} B_{\lambda}(T_{\text{dust}}) \kappa(a)}{D^2} \quad (1)$$

where  $M_{\text{dust}}^{\text{obs}}$  is the observed dust mass,  $T_{\text{dust}}$  is the dust temperature,  $B_{\lambda}(T_d)$  is the Planck function,  $\kappa(a)$  is the dust mass absorption coefficient (see Sarangi 2022 for the values used in this work),  $a$  is the grain radius, and  $D$  is the distance to the source from the observer. Since *WISE* only has two photometry points at each epoch, we are limited to using one temperature component and one dust composition. We also choose a pure graphite composition with single-size grains of  $a = 0.1 \mu\text{m}$  following Fox et al. (2010, 2011). We note that at early time ( $\lesssim 200$  days), the SN light still dominates the emission in mid-IR and the results from SED fitting in those epochs could only be an upper limit of the measured dust properties. We also note that the W1 ( $3.4 \mu\text{m}$ ) band can be contaminated by the PAH emission and the W2 band ( $4.6 \mu\text{m}$ ) band can be contaminated by carbon monoxide (CO) emission at  $4.65 \mu\text{m}$ .

We fit Equation (1) to our data using the method `curve-fit` in `SciPy` package (Virtanen et al. 2020), which varies fitting parameters to find the best fit to the data using the method of least squares (Jones 2001). Fig. 2 plots the best-fit dust models for the four longer-lived SNe (ASASSN-15kj, SN 2016gkg, SN 2017faa and SN 2017hpc). Table 3 lists the dust parameters of all SNe from the best SED fitting.

We also worked out the minimum shell size of an observed dust component, by assuming that the observed flux is a perfect blackbody (BB) as in Fox et al. (2011), so that

$$R_{\text{BB}}(t) = \sqrt{\frac{L}{4\pi\sigma T^4}} = \sqrt{\frac{4\pi d^2 \int F_{\lambda}^{\text{obs}} d\lambda}{4\pi\sigma T^4}} \quad (2)$$

where  $\sigma$  is Stefan-Boltzmann's constant. The measured black body radius  $R_{\text{BB}}$  at each epoch are also listed in Table 3.

In addition, the shock radius  $r_s \sim v_s t$ , for a constant shock velocity  $v_s$ , defines the maximum radius that the forward shock can travel in a time  $t$ . The associated dust mass processed by the forward shock of the SN is given by Equation (6) in Fox et al. (2011), assuming a dust to gas ratio of 0.01:

$$M_{\text{d}}(M_{\odot}) \approx 0.0028 \left( \frac{v_s}{15,000 \text{ km s}^{-1}} \right)^3 \left( \frac{t}{\text{yr}} \right)^2 \left( \frac{a}{\mu\text{m}} \right) \quad (3)$$

where  $v_s$  is the shock velocity,  $t$  is the time post explosion, and  $a$  is the dust grain size. The shock velocity corresponds to the broad component of optical spectral line width, which is typically  $\sim 5000$  to  $15000 \text{ km s}^{-1}$  for CCSNe.

The mid-IR emission has been explained with the presence of newly formed dust, or pre-existing dust heated by the radiation from the SN or CSM interactions (Fransson et al. 2014; Fox et al. 2015). As discussed in Tinyanont et al. (2016) and Szalai et al. (2019), the shocked dust mass can distinguish these two scenarios as shown in Fig. 3. If the mass derived from SED fitting is larger than the predicted shocked dust mass even at the highest shock velocity of  $15000 \text{ km s}^{-1}$ , the dust is pre-existing at the time of the explosion and radiatively heated by ongoing CSM interactions. In contrast, the dust is newly formed either in ejecta or a cool dense shell (CDS) behind the forward shock when  $R_{\text{BB}}$  is smaller than the shock radius  $r_s$  at the lowest shock velocity of  $5000 \text{ km s}^{-1}$ . While in cases where  $R_{\text{BB}}$  is between the shock radius  $r_s$  at the shock velocity of  $5000 \text{ km s}^{-1}$  and  $15000 \text{ km s}^{-1}$ , the dust radius is consistent with the shock front, suggesting that new dust may be forming in the CDS behind the forward shock but the presence of pre-existing dust should be still invoked to explain the amount of observed mid-IR radiations. Therefore, the origin of most SN dust in our sample are pre-existing dust dominated, and newly formed dust was definitely formed in 2003gd and SN 2016gkg at the last epoch considering the errors.

We also noted that the SN dust varied from  $10^{-5}$  to  $10^{-2} M_{\odot}$  and can dominate the mid-IR emission of CCSNe from quite early time around 100 days up to 1000 days, with most of them clustered within 400 days post

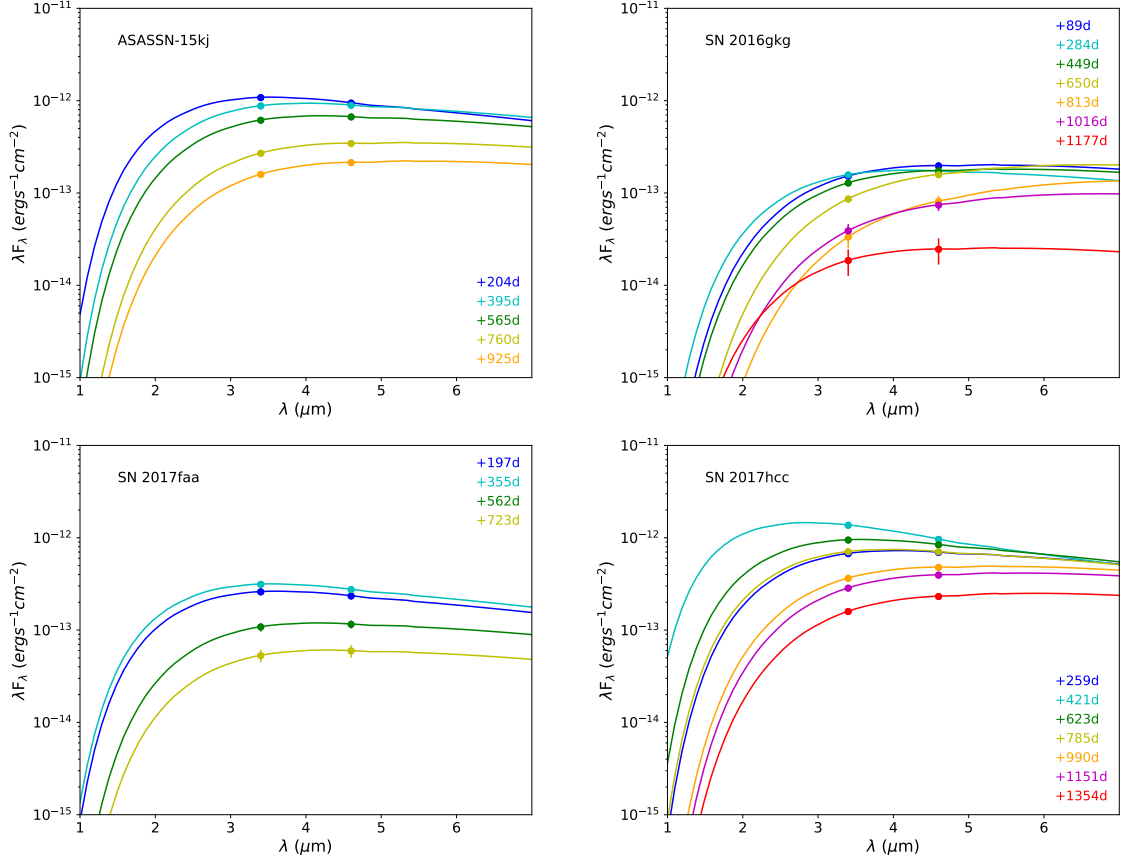


**Figure 2.** SEDs of ASASSN-15kj, SN 2016gkg, SN 2017faa and SN 2017hpc at different epochs. *WISE* data are plotted in circles, and the overplotted lines are the best fit dust models following Equation (1).

discovery which is consistent with the result of *Spitzer* (Szalai et al. 2019). The dust radius marked by  $R_{\text{BB}}$  extended from  $10^{15}$  to the order of  $10^{16}$  cm, sharing similar distribution with the result of *Spitzer*. However, the *Spitzer* sample presents a wider range of SN dust in both epochs and the amount of dust mass and radius. In addition, studies of Shahbandeh et al. (2023); Zsíros et al. (2024); Szalai et al. (2025) have also found a significant amount of newly formed dust in the ejecta even tens of years after explosion based on *JWST* data at longer wavelength. Therefore, the bias of the measured SN dust in our sample can be primarily due to wavelength limitation of *WISE* which is insensitivity to cold dust with  $T_{\text{dust}} \lesssim 400\text{K}$ . Since we study the environmental properties of the dusty SNe by comparing them with the entire IFS sample, this bias has a limited impact on our results discussed in the following sections. On the other hand, the comparison of the SN dust within the H-rich, H-poor and type IIin dusty SNe suggests that these three SN types show no significant difference in SN dust mass, radius and epochs.

### 3. ENVIRONMENTAL PROPERTIES

In this section, we analyze the local environment of dusty SNe in our sample and compare the properties between the different CCSN types. The median and mean values of the environmental properties of dusty SNe are listed in Table 2. We note a clear difference in  $H\alpha$  equivalent width, metallicity, star formation rate and Extinction between dusty and typical SN types, which would be discussed more in detail in the following.

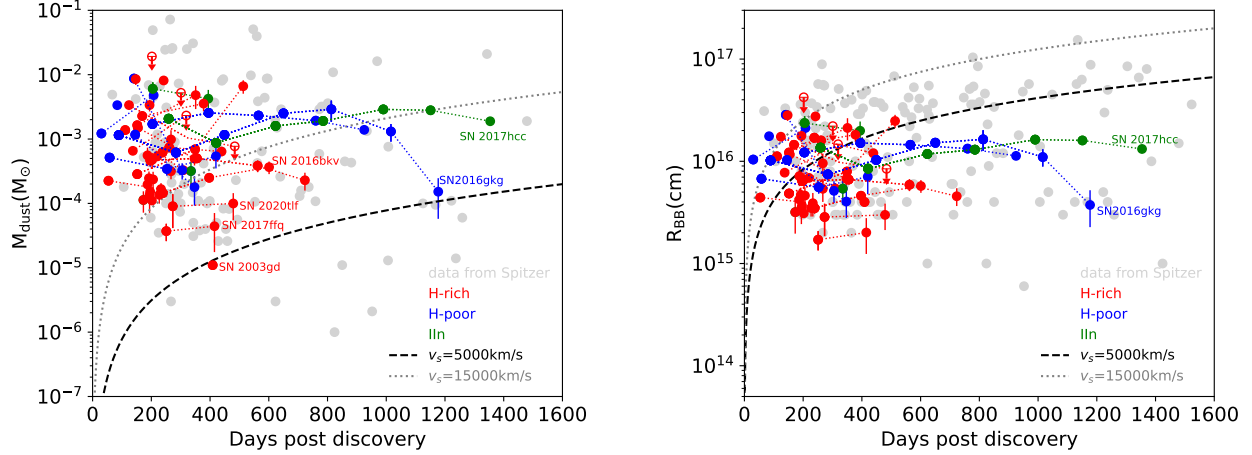
#### 3.1. $H\alpha$ equivalent width

Figure 4 shows the cumulative distributions of  $\text{EW}(H\alpha)$  of the SN-hosted HII regions for different CCSN types, and the KS test for each combination of them. We note that dusty SNe as a whole has a relatively higher  $\text{EW}(H\alpha)$  compared to the typical SN types which share a similar distribution in  $\text{EW}(H\alpha)$ , which indicates a connection of dusty SNe with younger stellar populations. The differences of the distribution for each

**Table 1.** The local environmental properties of the 42 dusty SNe studied in this work.

Name	Type	Distance	EW(H $\alpha$ )	12+log(O/H) <sub>D16</sub>	log $\Sigma_{\text{SFR}}$	E(B-V)	References
		Mpc	Å		M $_{\odot}\text{yr}^{-1}\text{kpc}^{-2}$	mag	
SN 2003gd	IIP	8.97	43.18 $\pm$ 3.01	8.49 $\pm$ 0.01	-2.241 $\pm$ 0.021	0.003 $\pm$ 0.121	Van Dyk et al. (2003)
SN 2010dr	IIL	78.77	30.02 $\pm$ 2.96	8.31 $\pm$ 0.02	-2.282 $\pm$ 0.034	0.255 $\pm$ 0.217	Kinugasa & Takahashi (2010)
SN 2013ej	IIP	8.97	17.59 $\pm$ 1.20	8.73 $\pm$ 0.02	1.065 $\pm$ 0.021	1.008 $\pm$ 0.727	Valenti et al. (2014)
SN 2014az	IIP	59.89	44.77 $\pm$ 1.38	8.01 $\pm$ 0.01	-2.300 $\pm$ 0.033	0.114 $\pm$ 0.227	Parker et al. (2014)
SN 2014ay	II	46.47	39.25 $\pm$ 1.17	8.31 $\pm$ 0.02	-1.873 $\pm$ 0.000	0.358 $\pm$ 0.083	Holoien et al. (2014)
ASASSN-14az	I Ib	31.34	25.48 $\pm$ 1.08	7.86 $\pm$ 0.09	-2.379 $\pm$ 0.000	-	Benetti et al. (2014)
SN 2014cw	II	40.23	-	8.09 $\pm$ 0.14	-2.822 $\pm$ 0.000	0.279 $\pm$ 0.288	Elias-Rosa et al. (2014)
ASASSN-14ma	IIP	58.54	64.85 $\pm$ 2.31	8.10 $\pm$ 0.02	-1.637 $\pm$ 0.000	0.152 $\pm$ 0.041	Cao et al. (2014)
ASASSN-15ab	I In	78.32	313.14 $\pm$ 1.23	8.38 $\pm$ 0.01	-3.347 $\pm$ 0.001	0.130 $\pm$ 0.010	Shappee et al. (2015a)
ASASSN-15jp	II	42.01	48.08 $\pm$ 3.20	8.28 $\pm$ 0.04	-2.455 $\pm$ 0.000	0.422	Falco et al. (2015)
ASASSN-15kj	Ic	82.38	44.94 $\pm$ 1.14	8.61 $\pm$ 0.01	-1.943 $\pm$ 0.000	0.266 $\pm$ 0.045	Shappee & Morrell (2015)
ASASSN-15ln	II	67.06	-	8.12 $\pm$ 0.10	-2.342 $\pm$ 0.000	0.202 $\pm$ 0.152	Benetti et al. (2015)
ASASSN-15ng	IIP	44.23	130.49 $\pm$ 3.25	8.25 $\pm$ 0.01	-1.269 $\pm$ 0.001	0.235 $\pm$ 0.025	Shappee et al. (2015b)
SN 2015bj	II	50.04	40.11 $\pm$ 1.91	8.35 $\pm$ 0.02	-2.082 $\pm$ 0.000	0.203 $\pm$ 0.070	Galbany et al. (2016a)
SN 2016B	IIP	19.38	86.01 $\pm$ 2.30	7.90 $\pm$ 0.02	-1.467 $\pm$ 0.001	0.082 $\pm$ 0.024	Piasek & Steele (2016)
SN 2016C	IIP	20.26	14.69 $\pm$ 1.16	8.43 $\pm$ 0.04	-2.738 $\pm$ 0.000	-	Sahu et al. (2016)
SN 2016X	IIP	18.05	58.98 $\pm$ 3.41	8.01 $\pm$ 0.04	-2.437 $\pm$ 0.000	0.203 $\pm$ 0.100	Zheng & Zhang (2016)
SN 2016aqf	IIP	17.61	121.12 $\pm$ 4.16	7.84 $\pm$ 0.03	-1.139 $\pm$ 0.001	0.098 $\pm$ 0.033	Ryder et al. (2016)
SN 2016bkv	IIP	8.79	6.54 $\pm$ 0.52	8.77 $\pm$ 0.02	-2.336 $\pm$ 0.024	0.429 $\pm$ 0.204	Hosseinzadeh et al. (2018)
SN 2016blz	II	51.83	69.73 $\pm$ 2.00	7.89 $\pm$ 0.04	-1.424 $\pm$ 0.001	0.294 $\pm$ 0.056	Magee et al. (2016a)
SN 2016bmi	II	33.12	15.88 $\pm$ 1.93	8.19 $\pm$ 0.14	-2.838 $\pm$ 0.000	-	Magee et al. (2016b)
SN 2016cdd	Ib	38.05	994.94 $\pm$ 20.23	8.09 $\pm$ 0.03	0.314 $\pm$ 0.152	0.248 $\pm$ 0.036	Hosseinzadeh et al. (2016)
SN 2016cvk	I In	47.81	24.37 $\pm$ 0.26	8.60 $\pm$ 0.04	-4.041 $\pm$ 0.010	0.150 $\pm$ 0.020	Bersier et al. (2016)
SN 2016cyx	II	60.78	196.10 $\pm$ 5.39	8.55 $\pm$ 0.01	-1.025 $\pm$ 0.002	0.165 $\pm$ 0.028	Falco et al. (2016)
SN 2016gkg	I Ib	21.59	-	8.78 $\pm$ 0.06	-3.600 $\pm$ 0.000	- $\pm$ 0.384	Van Dyk et al. (2016)
SN 2016hgm	II	33.56	148.06 $\pm$ 5.33	8.36 $\pm$ 0.01	-1.372 $\pm$ 0.001	0.256 $\pm$ 0.033	Dimitriadis et al. (2016)
SN 2016hwn	II	96.42	19.86 $\pm$ 5.77	8.28 $\pm$ 0.09	-2.867 $\pm$ 0.000	-	Bersier (2016)
SN 2016iae	Ic	15.41	317.28 $\pm$ 13.39	8.77 $\pm$ 0.03	-0.895 $\pm$ 0.003	1.019 $\pm$ 0.229	Jha et al. (2016)
SN 2017bzb	II	12.75	121.74 $\pm$ 18.71	8.04 $\pm$ 0.05	-2.425 $\pm$ 0.000	0.066 $\pm$ 0.097	Morrell et al. (2017)
SN 2017faa	II	82.38	-	8.48 $\pm$ 0.01	-1.931 $\pm$ 0.000	0.229 $\pm$ 0.024	Somero et al. (2017)
SN 2017fbu	II	48.25	120.19 $\pm$ 6.59	8.20 $\pm$ 0.02	-2.173 $\pm$ 0.000	0.067 $\pm$ 0.032	Rodriguez & Prieto (2017a)
SN 2017ffq	II	55.85	74.11 $\pm$ 1.91	8.51 $\pm$ 0.01	-0.948 $\pm$ 0.003	0.315 $\pm$ 0.047	Rodriguez & Prieto (2017b)
SN 2017fqk	II	45.13	79.26 $\pm$ 3.84	8.63 $\pm$ 0.02	-2.132 $\pm$ 0.000	0.419 $\pm$ 0.115	Tartaglia et al. (2017)
SN 2017gax	Ibc	20.71	84.55 $\pm$ 2.48	8.85 $\pm$ 0.01	-1.840 $\pm$ 0.000	0.363 $\pm$ 0.036	Jha et al. (2017)
SN 2017gmr	IIP	22.03	57.65 $\pm$ 2.35	8.42 $\pm$ 0.02	-1.922 $\pm$ 0.000	0.322 $\pm$ 0.055	Andrews et al. (2019)
SN 2017hcc	I In	74.71	13.44 $\pm$ 0.59	7.88 $\pm$ 0.10	-3.338 $\pm$ 0.000	0.249 $\pm$ 0.232	Dong et al. (2017)
SN 2017hpi	II	24.69	-	8.39 $\pm$ 0.04	-2.341 $\pm$ 0.000	0.212 $\pm$ 0.139	O'Neill et al. (2017)
SN 2017ivv	II/I Ib*	24.25	62.32 $\pm$ 6.13	8.30 $\pm$ 0.10	-2.659 $\pm$ 0.000	0.058 $\pm$ 0.082	Gutiérrez et al. (2020)
SN 2018pq	IIP	30.45	-	8.71 $\pm$ 0.01	0.180 $\pm$ 0.213	0.394 $\pm$ 0.044	Dubey et al. (2025)
SN 2018bbl	II	26.46	14.17 $\pm$ 1.08	8.49 $\pm$ 0.06	-2.975 $\pm$ 0.000	0.236 $\pm$ 0.186	Cartier et al. (2018)
SN 2018cuf	II	46.47	48.97 $\pm$ 1.36	8.67 $\pm$ 0.03	-2.350 $\pm$ 0.000	0.254 $\pm$ 0.074	Jha et al. (2018)
SN 2020tlf	IIP/L	37.56	115.73 $\pm$ 0.33	8.23 $\pm$ 0.05	-1.209 $\pm$ 0.031	0.064 $\pm$ 0.033	Jacobson-Galán et al. (2022)

NOTE—All the supernova types, distances and environmental parameters are taken from the IFU sample of G18 (Galbany et al. 2018), P23 (Pessi et al. 2023a) and M23 (Moriya et al. 2023). \*As discussed by Gutiérrez et al. (2020), SN2017ivv has a lower hydrogen mass than a typical SN II but more than a SN Ib, we included it in the group of H-poor SNe and labeled with II/Ib. (This table is available in machine-readable form.)



**Figure 3.** Dust mass ( $M_{\text{dust}}$ , left) and blackbody radius ( $R_{\text{BB}}$ , right) of dusty SNe derived from the SED fittings. Filled circles denote the dusty SNe with H-rich SNe in red, H-poor SNe in blue and type IIIn SNe in green, compared to the data from *Spitzer* (Szalai et al. 2019) in the filled circles of light gray. The empty symbols with downward arrows denote a upper limit in the measured dust mass. Dotted lines on the left panel denote theoretical dust masses at shock velocities  $v_s = 5000$  and  $15000$  km/s calculated by Equation (3).

**Table 2.** The median and mean value of the environmental properties of the three typical CCSN subtypes including all IFU samples and the dusty SN sample listed in Table 1.

Type	$\log \text{EW}(\text{H}\alpha)$	$12 + \log(\text{O}/\text{H})_{\text{D16}}$	$\log \Sigma_{\text{SFR}}$	E(B-V)
	$\text{\AA}$		$\text{M}_{\odot} \text{yr}^{-1} \text{kpc}^{-2}$	mag
	Median			
H-rich	1.57	8.58	-1.96	0.13
H-poor	1.56	8.59	-1.89	0.15
IIIn	1.58	8.57	-2.47	0.20
<b>Dusty SNe</b>	<b>1.77</b>	<b>8.33</b>	<b>-2.21</b>	<b>0.24</b>
<b>H-rich</b>	1.76	8.31	-2.15	0.23
<b>H-poor</b>	1.89	8.61	-1.94	0.27
<b>IIIn</b>	1.82	8.38	-3.55	0.16
	Mean			
H-rich	$1.74 \pm 0.57$	$8.54 \pm 0.32$	$-1.84 \pm 0.91$	$0.18 \pm 0.19$
H-poor	$1.66 \pm 0.58$	$8.58 \pm 0.26$	$-1.86 \pm 0.66$	$0.17 \pm 0.16$
IIIn	$1.76 \pm 0.66$	$8.50 \pm 0.29$	$-2.73 \pm 1.22$	$0.22 \pm 0.16$
<b>Dusty SNe</b>	<b><math>2.02 \pm 0.44</math></b>	<b><math>8.34 \pm 0.28</math></b>	<b><math>-2.02 \pm 1.01</math></b>	<b><math>0.27 \pm 0.21</math></b>
<b>H-rich</b>	$1.70 \pm 0.37$	$8.32 \pm 0.26$	$-1.88 \pm 0.87$	$0.25 \pm 0.19$
<b>H-poor</b>	$2.05 \pm 0.59$	$8.47 \pm 0.39$	$-1.86 \pm 1.26$	$0.39 \pm 0.27$
<b>IIIn</b>	$1.77 \pm 0.64$	$8.35 \pm 0.27$	$-3.58 \pm 0.40$	$0.18 \pm 0.06$

NOTE—The environmental properties of dusty SNe in bold are presented in terms of the three typical SN types (H-rich, H-poor, and type IIIn), respectively. The values of dusty SNe in the three typical SN types are corrected based on the new SN type classification.

SN type combinations are also presented quantitatively in the KS matrix, and the  $p$ -value of the tests express the statistical significance of two distributions being drawn from the same parent sample. We choose a confidence level of 95%, that is, we consider that a  $p$ -value  $\leq 0.05$  as indicating a statistically significant difference between these two distributions. Therefore, dusty SNe show statistically significant differences with hydrogen-rich SNe in terms of  $\text{EW}(\text{H}\alpha)$ , although more than 60% of dusty SNe are hydrogen-rich ones.

In Figure 5, we further study the  $\text{EW}(\text{H}\alpha)$  of dusty SN hosts in different types, H-rich, H-poor and IIIn respectively. In general, dusty SN hosts prefer the location of higher  $\text{H}\alpha$  equivalent width in all subtypes, and this preference increases from H-rich, type IIIn and to H-poor. Considering the meaning of  $\text{EW}(\text{H}\alpha)$  as stellar age indicator, the increasing sequence from H-rich, type IIIn to H-poor indicates the decrease of average age, which is consistent with the predicted stellar age of the corresponding SN progenitors (Smartt 2009, 2015).

### 3.2. Star formation rate

Figure 6 presents the cumulative distributions of SFR intensity in the SN host HII regions for different SN subtypes and the KS test of each combination. H-rich and H-poor SNe show a similar distribution of star formation rate and tend to occur at higher SFR regions, followed by dusty SNe and type IIIn SNe. There is an increasing deviation for the SFR distributions of different types as the host SFR decreases, in particular for type IIIn SNe. The significant difference in SFR between type IIIn with H-rich and H-poor SNe are also presented in the KS test matrix of  $p$ -value  $< 0.05$ . The dusty SNe again statistically differs with H-poor SNe in terms of star formation rate with a relatively lower SFR, but do not have a statistically significant difference with type IIIn and H-rich SNe any more as shown in the KS matrix.

In Figure 7, the SFR distribution of dusty SN hosts in three typical SN types are presented. We note that H-rich and H-poor dusty SNe span a similar distribution with the corresponding typical SN types. On the other hand, the type IIIn dusty SNe are more likely discovered at lower star formation rate regions compared to the typical type. In general, H-rich and H-poor SNe are more correlated with ongoing massive star formation than IIIn SNe. Type IIIn SNe contribute to more dust at the region of lower SFR than other CCSN types. Considering that the sample of type IIIn dusty SNe is small, it is difficult to draw any definitive conclusions about the overall trend.

We also note that there are inconsistencies between the  $\text{EW}(\text{H}\alpha)$  and SFR distributions, and it would be necessary to investigate the physical processes described by these two parameters. The star formation rate intensity  $\log\Sigma_{\text{SFR}}$  here is measured from the extinction-corrected  $\text{H}\alpha$  flux contributed by young massive stars, tracing the ongoing SFR.  $\text{EW}(\text{H}\alpha)$  is measured by the strength of the line relative to the continuum, which in fact can be an indicator of the strength of the ongoing SFR compared with the past SFR, which reduces with time if no new stars are created. However, considering the size of HII region segregation in IFS can be as large as hundreds of parsec in radius, the continuous star formation bursts in the same site are more reasonable, compared to a single instantaneous star formation history. Therefore, the contamination from older stellar populations together with effect of photo-leakage can bring uncertainties to the estimation of stellar population age (Sun et al. 2021).

### 3.3. Oxygen abundance

Metallicity plays a crucial role in the evolution of massive stars and their final CCSN explosions. Oxygen is the most abundant metal in the gas phase and exhibits very strong nebular lines at optical wavelengths, so that is usually chosen as a metallicity indicator. The cumulative distributions of oxygen abundance of the SN host HII regions for different SN subtypes and the KS test for each combination, are presented in Figure 8. The dusty SN hosts are located at lower metallicity regions with the mean and median values of  $12+\log(\text{O}/\text{H})_{\text{D16}} \sim 8.33$  dex, which is more than 0.2 dex lower than those of typical CCSN host regions as shown in Table 3. By contrast, the three typical CCSN hosts span a similar distribution in a range from  $12+\log(\text{O}/\text{H})_{\text{D16}} \sim 8.0$  to 8.8 dex. Additionally, the KS test with  $p$ -value  $< 0.05$  also suggests that there is statistically significant difference between dusty SNe and the typical CCSN types in oxygen abundance.

In Figure 9, we further compare the oxygen abundance of dusty SN hosts in different types, H-rich, H-poor and IIIn respectively. We find that compared to the typical types, the distributions of H-rich and type IIIn dusty SNe are shifted to lower metallicity regions, while H-poor dusty SNe span a similar range. As a consequence, a clear sequence in terms of average metallicity from low to high emerges, H-rich, type IIIn and H-poor. This may indicate that H-poor dusty SNe are less sensitive with metallicity, and turn out to be the main dust contributor in higher metallicity regions. Considering the effect of metallicity on mass loss history of SN progenitors which

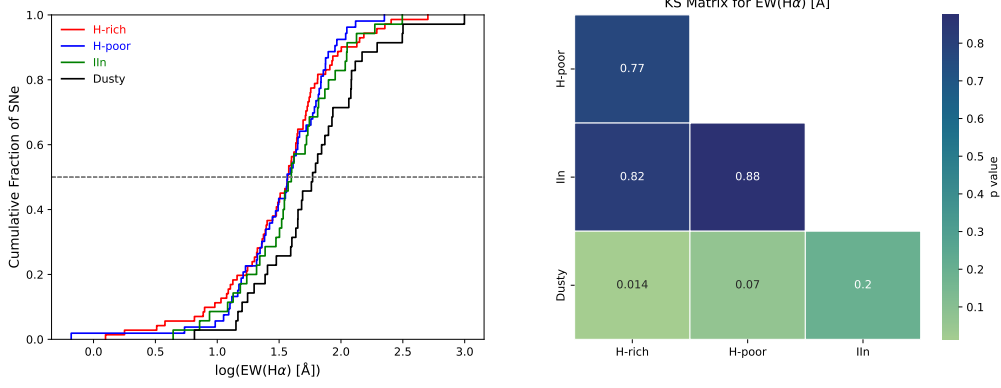


**Figure 4.** Left: normalized cumulative distributions of H $\alpha$  equivalent width of SN hosted HII regions in four types: H-rich in blue, H-poor in red, IIn in green and dusty SNe in black. A dotted horizontal line at 0.5 fraction represents the median value of the distributions. Right: KS matrix for each combination of different SN types.

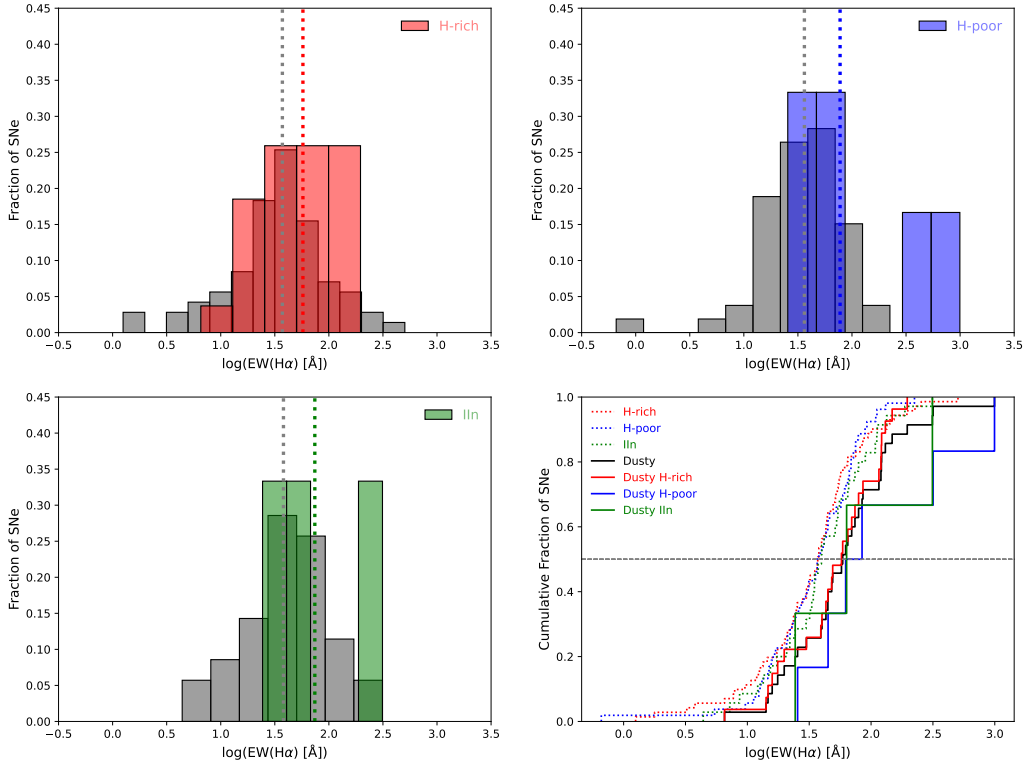


**Figure 5.** Histograms of H $\alpha$  equivalent width of dusty SNe in three types: H-rich in blue (the top left), H-poor in red (the top right), and IIn in green (the bottom left) separately, compared with typical SN types in gray. The median values of different SNe types are marked by the vertical lines. In the bottom right, the normalized cumulative distributions are compared between typical SNe in dotted lines and dusty SNe in solid lines.

construct the CSM surrounding SNe, the difference in metallicity of different dusty SN types may reflect the diversity in the evolution of the corresponding SN progenitors. H-rich SNe are usually thought to arise from massive stars experiencing a single-star evolution, whose mass loss are metallicity dependent driven by stellar wind. By contrast, H-poor SN progenitors are more dominated by lower-mass stars in binary systems

with mass loss through binary interactions, which is less dependent on metallicity (Eldridge et al. 2017). The progenitor populations of type IIn SNe can be a combination of both single and binary star system, so that its metallicity is in the middle between H-rich and H-poor SNe.

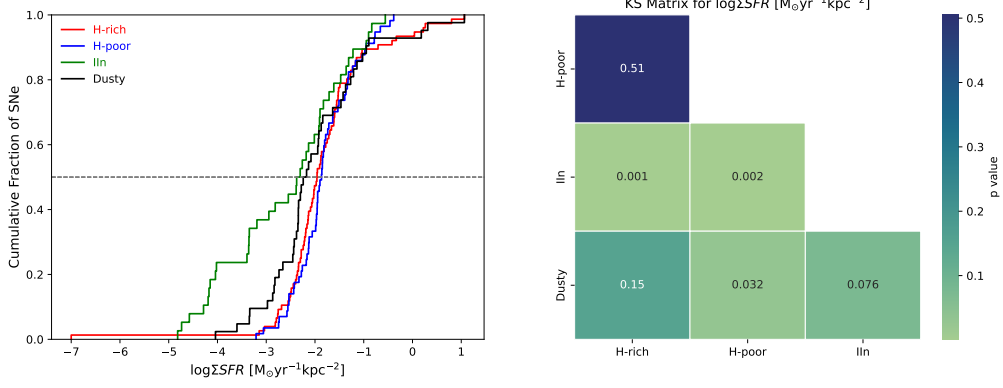


**Figure 6.** Left: normalized cumulative distributions of star formation rate intensity at SN sites are compared between dusty SNe in black and three typical SN types with H-rich in blue, H-poor in red, and IIn in green. A dotted horizontal line at 0.5 fraction represents the median value of the distributions. Right: KS statistic matrix for each combination of SN types.

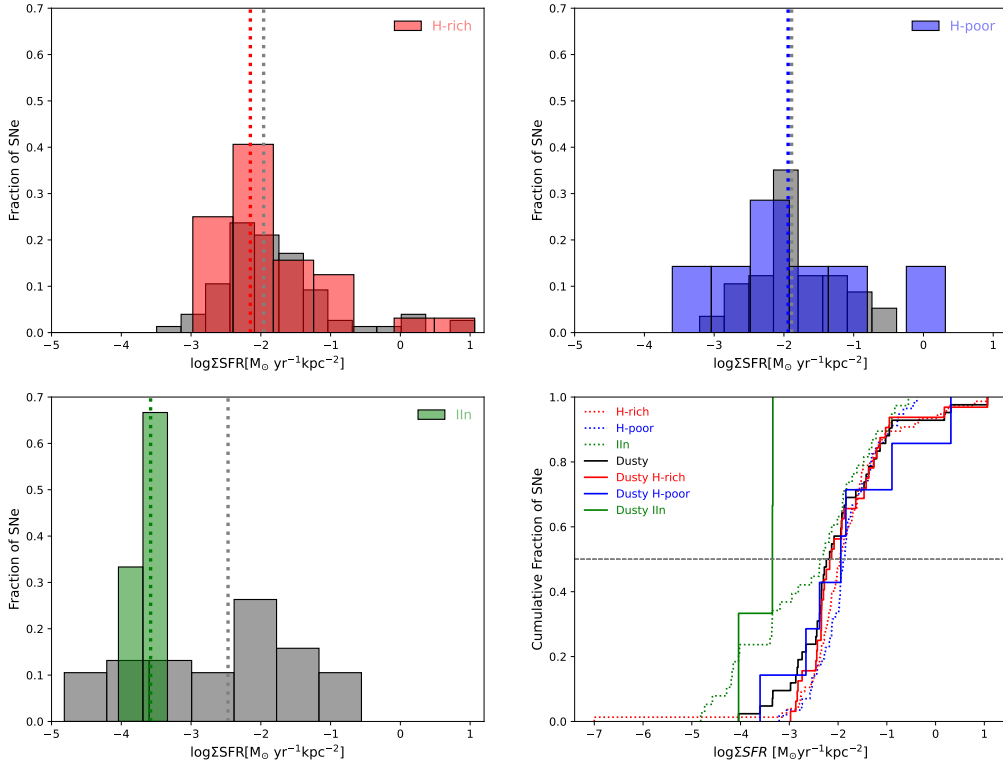


**Figure 7.** Histograms of star formation rate (SFR) of dusty SNe in three types: H-rich in blue (the top left), H-poor in red (the top right), and IIn in green (the bottom left) separately, compared with typical SN types in gray. The median values of different SNe types are marked by the vertical lines. In the bottom right, the normalized cumulative distributions are compared between typical SNe in dotted lines and dusty SNe in solid lines.

### 3.4. Extinction

The extinction for SN host HII regions is also related to the extinction suffered by the SN themselves. We therefore compare the values of extinction between dusty SNe with the different CCSN types and analyze which subtype environment is more reddened, and therefore more affected by the presence of pre-existing dust. Fig-

ure 10 presents the cumulative distributions for the SN host extinction in different SN types and reported the KS matrix for each combination of them. We note that dusty SNe have a similar distribution with the traditionally CSM-interaction SNe, type IIn, which are more likely located at higher extinction regions. On the other hand, H-rich and H-poor SNe also share a similar range in extinction but with lower values of  $E(B-V)$ . There-

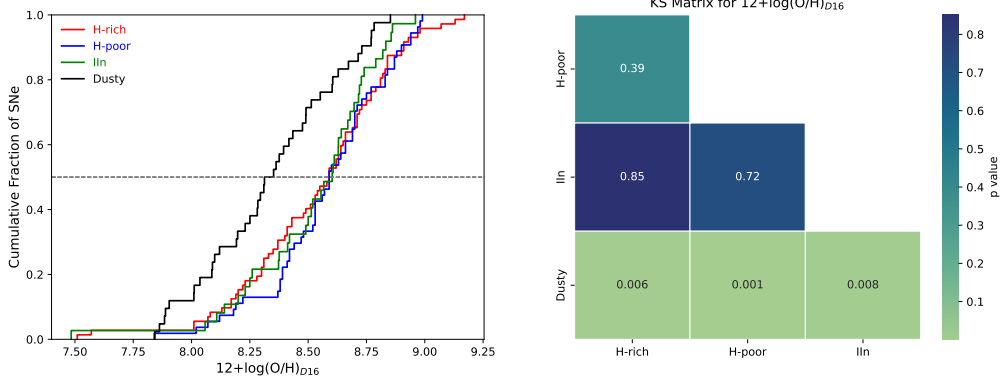


**Figure 8.** Left: normalized cumulative distributions of oxygen abundance ( $12+\log(\text{O}/\text{H})_{\text{D16}}$ ) at SN sites are compared between dusty SNe in black and three typical SN types with H-rich in blue, H-poor in red, and IIn in green. A dotted horizontal line at 0.5 fraction represents the median value of the distributions. Right: KS statistic matrix for each combination of SN types.

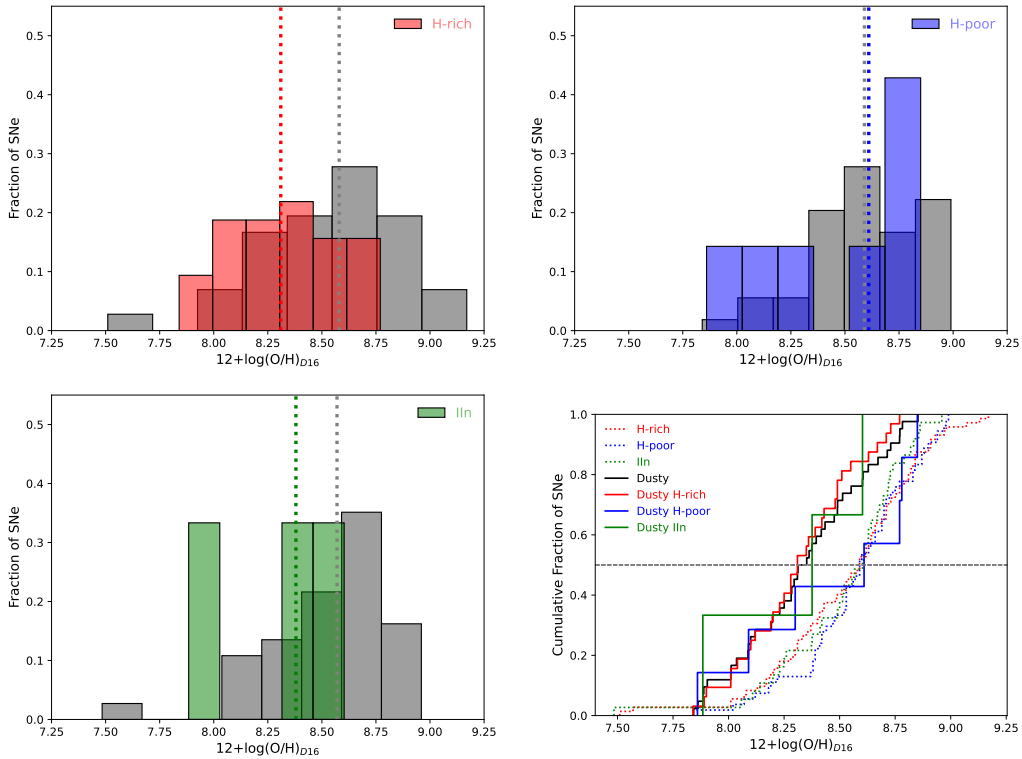


**Figure 9.** Histograms of oxygen abundance ( $12+\log(\text{O}/\text{H})_{\text{D16}}$ ) of dusty SNe in three types: H-rich in blue (the top left), H-poor in red (the top right), and IIn in green (the bottom left) separately, compared with typical SN types in gray. The median values of different SNe types are marked by the vertical lines. In the bottom right, the normalized cumulative distributions are compared between typical SNe in dotted lines and dusty SNe in solid lines.

fore, the SN dust formation may correlate to higher extinction host environments, where CSM interactions are more effective.

Then, the KS matrix with  $p$ -value  $< 0.05$  in the combination of type IIn and dusty with H-rich and H-poor SNe, suggests a statistically significant difference between these types. In addition, Figure 11 presents the extinction difference of dusty SN host environment in

different types. We note that most dusty SNe shift to higher extinction region, redexcept for type IIn dusty SNe which host at lower extinction region. Therefore, it seems to be critical for H-rich and H-poor SNe to explode in a more dusty environment to become an observed dusty SNe in mid-IR. In fact, the mid-IR studies have revealed that a significant amount of newly-formed dust in SN ejecta and SN shocked regions is attributed

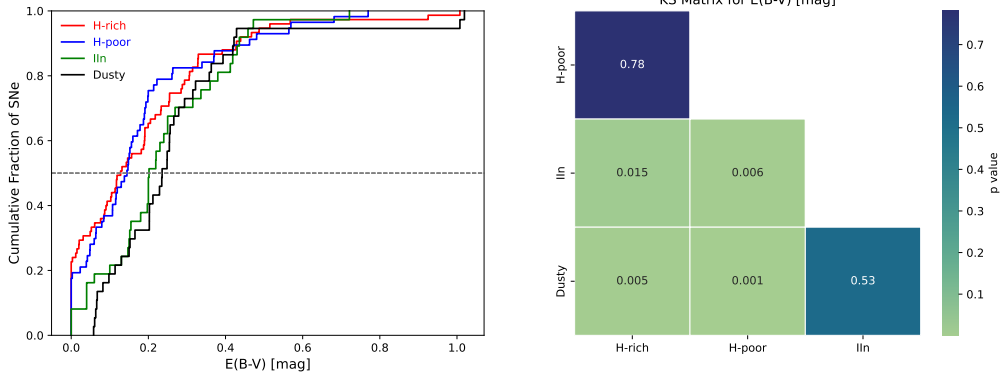


**Figure 10.** Left: normalized cumulative distributions of  $E(B-V)$  at SN sites are compared between dusty SNe in black and three typical SN types with H-rich in blue, H-poor in red, and IIin in green. A dotted horizontal line at 0.5 fraction represent the median value of the distributions. Right: KS statistic matrix for each combination of SN types.

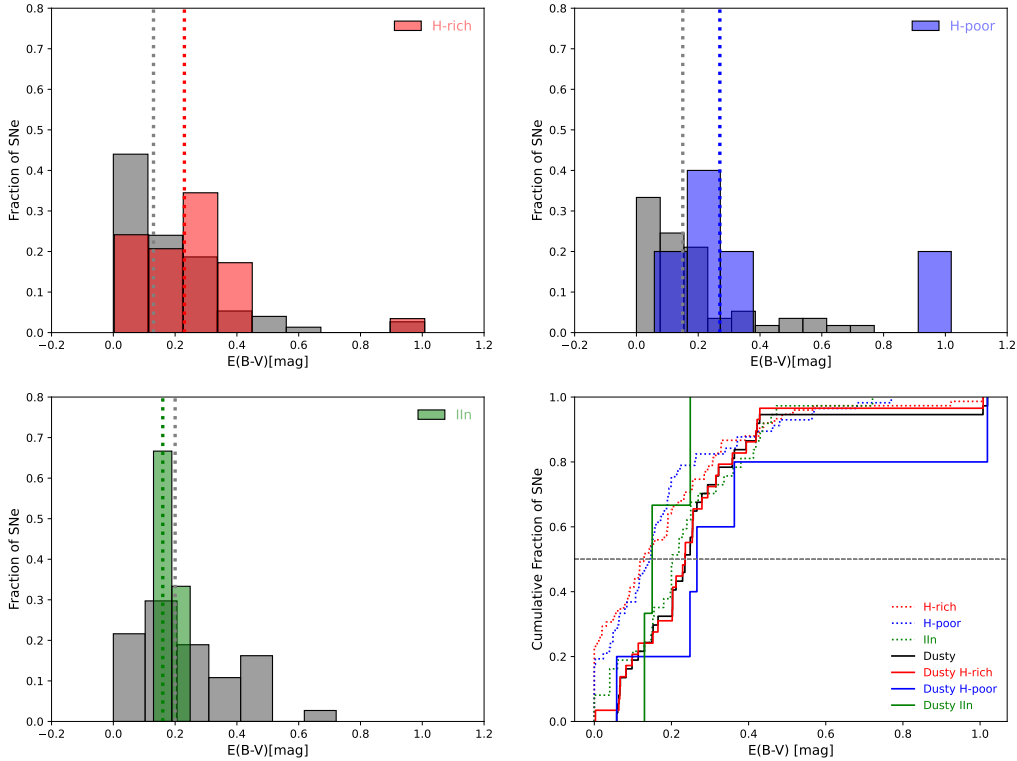


**Figure 11.** Histograms of  $E(B-V)$  of dusty SNe in three types: H-rich in blue (the top left), H-poor in red (the top right), and IIin in green (the bottom left) separately, compared with typical SN types in gray. The median values of different SNe types are marked by the vertical lines. In the bottom right, the normalized cumulative distributions are compared between typical SNe in dotted lines and dusty SNe in solid lines.

to the observed luminous mid-IR emissions (Fox et al. 2011; Szalai & Vinkó 2013; Smith 2017).

#### 4. ENVIRONMENTAL DEPENDENCE OF SN DUST

For each SN, we use the data at the epoch with the largest measured dust mass as their dust contribution

labeled in bold in Table 3, and investigated whether there is any correlation between SN dust and host environmental properties. We employed PyMC3 (Salvatier J 2016) for a Bayesian regression assuming Gaussian uncertainties for the environmental parameters, and evaluated the Pearson correlation coefficient  $\rho$  and  $p$ -value to determine the existence and the strength of correlations. Given the small number of the dusty SNe in H-poor and

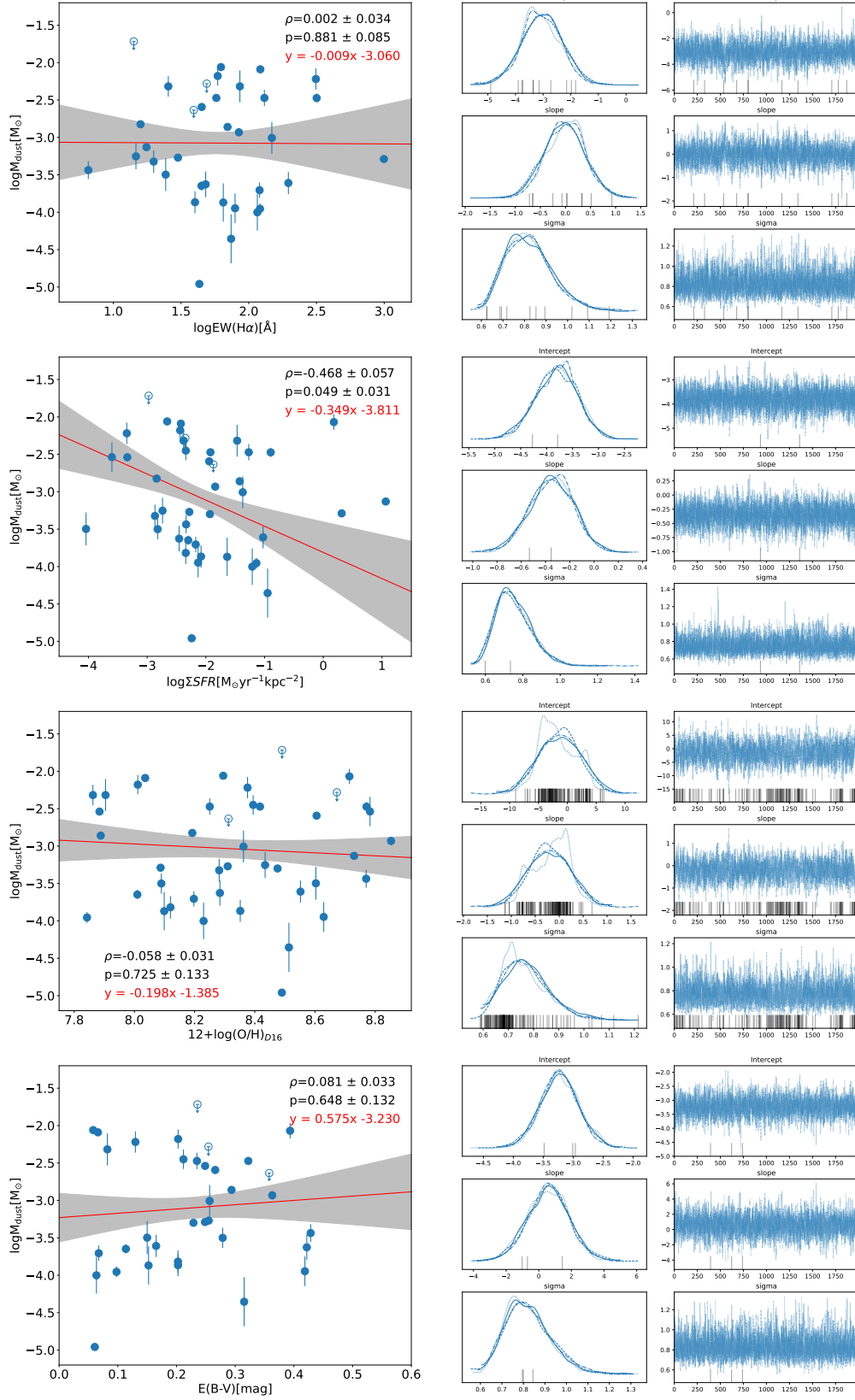


**Figure 12.** The correlation between the largest dust mass  $M_{\text{dust}}$  of each SN labeled in bold in Table 3 and the four environmental properties with EW(H $\alpha$ ), star formation rate intensity, oxygen abundance, and E(B-V). The left panels show the result of Bayesian regression in the red line with a  $1-\sigma$  uncertainty in the gray shades. Each Pearson correlation coefficient  $\rho$  and  $p$ -value is shown along with its standard deviation. The posterior distributions of the fitting parameters are presented in the left panels.

type IIn, we did not distinguish SN types and used the whole dusty SN sample to do the simulation.

Figure 12 presents the result of the linear regression between the SN dust mass and the four environmental properties and posterior distribution of the fitting parameters. We note that one marginal correlation is a negative correlation between the dust mass and star formation rate, according to the Pearson test of correlation coefficient  $\rho = -0.468 \pm 0.057$  and  $p$ -value = 0.049  $\pm$  0.031. This means that SNe would be more mid-IR luminous and more dust-rich at the region of lower star formation rate. Unlike SFR, there is no correlation between EW(H $\alpha$ ) and SN dust mass, with a very low correlation coefficient  $\rho = 0.002 \pm 0.034$  ( $p$ -value = 0.881  $\pm$  0.085). In addition, it is worth noting that we did not find significant correlations between SN dust mass and metallicity and host extinction with lower correlation coefficient  $\rho = 0.058 \pm 0.031$  and  $0.081 \pm 0.033$  ( $p$ -value = 0.725  $\pm$  0.133 and 0.648  $\pm$  0.132) respectively, which were thought to be key factors affecting the mass-loss history of progenitors and the CSM environment of SNe. It seems that the formation process of SN dust is less dependent on metallicities, which is consistent with the findings of [Moriya et al. \(2023\)](#) for type IIn SNe. The mid-IR emission used for the measurement of SN dust mass is insensitive to the interstellar extinction, and can be a reasonable explanation for this result.

## 5. CONCLUSIONS

In this work, we discovered 42 mid-IR luminous dusty SNe with local IFS data based on *Spitzer* and *WISE* images. The observed mid-IR emission indicates the presence of newly formed dust, or pre-existing dust heated by the radiation from the SN or CSM interactions. We carried out a systematic analysis of the SN host environments and their dust properties, for understanding the dust-veiled exploding stars, and whether SN dust formation is associated with the local environments. Our main conclusions have been summarized as follows.

1. We note a clear difference in the host environments of dusty SNe compared to typical CCSN types. Dusty SNe prefer the locations with higher EW(H $\alpha$ ), lower metallicity, and heavier host extinctions, which indicate that they may come from younger and higher-mass progenitors.
2. Dusty SNe in different subtypes show diversities in terms of their host environmental properties. We found the same increasing sequence in the values

of EW(H $\alpha$ ) and oxygen abundance from H-rich, type IIn to H-poor dusty SNe. These differences in subtypes of dusty SNe reflect the diversity of their progenitors. The progenitors of H-poor dusty SNe seem to be mostly sensitive with their host environments.

3. Based on the mid-IR fitting results, we found that the pre-existing dust can dominate the mid-IR emission of CCSNe from quite early time around 100 days up to 1000 days post discovery, which become the main source of the observed dust in our sample CCSNe.
4. We found that one marginal correlation is a negative correlation between the dust mass and star formation rate. This means that SNe would be more mid-IR luminous and more dust-rich at the region with lower star formation rate.
5. We did not find significant correlations of the SN dust mass with the metallicity and the host extinction, which were thought to be key factors affecting the mass-loss history of progenitors and the CSM environment of SNe. This may indicate that the dust formation process in SNe might be insensitive to metallicity and the dust condition of the host regions.

Overall, our studies illustrate that the environmental studies of dusty SNe offer a powerful approach to investigate the dust formation in SNe and their potential correlation with progenitor systems. It is possible that some bias exists in our sample and affects our result. The SN types and dust measured in our sample are limited by *WISE* in observation band, resolution and epochs. Future wide-field IR surveys increasing the amount and diversity of dusty SNe with less biases, could allow for an even better statistical sample for a systematic study. We expect more observational data and theoretical models to improve our understanding of dusty SNe and their environments. The photometry and spectrometry data from *JWST* can offer unprecedented opportunity to resolve the details of the immediate environment of the dusty SNe, trace the evolution of dust from SN to SN remnant phase, and test more precise dust models with different components [Sarangi \(2022\)](#); [Shahbandeh et al. \(2023\)](#); [Zsíros et al. \(2023\)](#).

We thank the referee for valuable comments. We thank all the people that have made this paper. LX is thankful for the support from National Natural Science Foundation of China (grant No. 12103050), Advanced Talents Incubation Program of the Hebei University, and Midwest Universities Comprehensive Strength Promotion project. L.G. acknowledges financial support from AGAUR, CSIC, MCIN and AEI 10.13039/501100011033 under projects PID2023-151307NB-I00, PIE 20215AT016, CEX2020-001058-M, ILINK23001, COOPB2304, and 2021-SGR-01270. Y.Y. appreciates the generous financial support provided to the supernova group at U.C. Berkeley by Gary and Cynthia Bengier, Clark and Sharon Winslow, Sanford Robertson, and numerous other donors. X.W. and Z.H. gratefully acknowledge the support provided by the NSFC under Grant No. 12288102.

This research is based on observations made with the Wide-field Infrared Survey Explorer (*WISE*) and the *Spitzer* Space Telescope, which are projects of the Jet Propulsion Laboratory, California Institute of Technology, and funded by the National Aeronautics and Space Administration and the National Science Foundation. We acknowledge the availability of unWISE services, which is a reprocessing of WISE data to improved depth and spatial resolution. This publication makes use of data products from the Centro Astronómico Hispano Alemán (CAHA) at Calar Alto, operated jointly by the Max-Planck-Institut für Astronomie (MPIA) and the Instituto de Astrofísica de Andalucía (CSIC), the European Southern Observatory under ESO programme(s): 096.D-0296 (A), 0103.D-0440 (A), 096.D-0263 (A), 097.B-0165 (A), 097.D-0408 (A), 0104.D-0503 (A), 60.A9301 (A), 096.D-0786 (A), 097.D-1054 (B), 0101.C-0329 (D), 0100.D-0341 (A), 1100.B-0651 (A), 094.B-0298 (A), 097.B-0640 (A), 0101.D-0748 (A), 095.D-0172 (A), 1100.B-0651 (A), 0100.D-0649 (F), 096.B-0309 (A), and SDSS-IV/MaNGA provided by the Alfred P. Sloan Foundation, the US Department of Energy Office of Science, and the Participating Institutions. SDSS-IV acknowledges support and resources from the Center for High Performance Computing at the University of Utah.

*Facilities:* *Spitzer/IRAC* (Fazio et al. 2004), *WISE* (Wright et al. 2010), *CAO:3.5m(PMAS/PPak)* (Verheijen et al. 2004), *VLT/MUSE* (Bacon et al. 2014), *APO:2.5m(SDSS)* (MaNGA; Bundy et al. 2015)

*Software:* *astropy* (Astropy Collaboration et al. 2013, 2018), *numpy* (Ferland et al. 2013), *SciPy* (Virtanen et al. 2020), *Matplotlib* (Bertin & Arnouts 1996), *Seaborns* (Waskom 2021), *Photutils* (Bradley et al. 2023), *SFFT* (Hu et al. 2021) *PyMC3* (Salvatier J 2016)

## APPENDIX

- A. THE REDSHIFT DISTRIBUTION OF THE IFS SAMPLE
- B. THE MID-IR PHOTOMETRY AND DUST PROPERTIES

Here, we present the mid-IR photometry and SED fitting results of the dusty SNe in our sample in Table 3. The data at epoch labeled in bold is used as the dust contribution of the SNe. The photometry of SN 2003gd and SN 2013ej

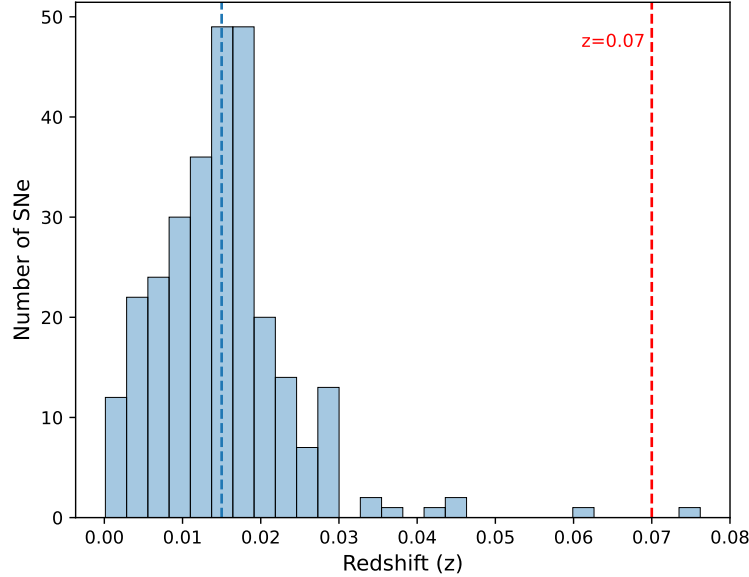


**Figure 13.** The redshift distribution of the IFS CCSN sample as the discussion in Section 2.1. The blue vertical line at  $z = 0.015$  is the median redshift of the CCSN IFS sample. The assumed detection limit of *WISE* is marked by the red vertical line of  $z = 0.07$  based on the observations of Myers et al. (2024).

are from *Spitzer* at  $3.5\mu\text{m}$  and  $4.5\mu\text{m}$ . The other SNe are detected by *WISE* at  $3.4\mu\text{m}$  and  $4.6\mu\text{m}$ . There are four SNe (SN 2014ay, SN 2017gmr, SN 2018bbl, SN 2018cuf), which at some epochs are only positively detected at  $4.6\mu\text{m}$ , so we calculated the flux with a  $3\sigma$  upper limit at  $3.4\mu\text{m}$  and upper limits for their corresponding dust parameters.

## REFERENCES

- Anderson, J. P., James, P. A., Haberman, S. M., Galbany, L., & Kuncarayakti, H. 2015, *PASA*, 32, e019, doi: [10.1017/pasa.2015.19](https://doi.org/10.1017/pasa.2015.19)
- Andrews, J. E., Krafton, K. M., Clayton, G. C., et al. 2016, *MNRAS*, 457, 3241, doi: [10.1093/mnras/stw164](https://doi.org/10.1093/mnras/stw164)
- Andrews, J. E., Sand, D. J., Valenti, S., et al. 2019, *ApJ*, 885, 43, doi: [10.3847/1538-4357/ab43e3](https://doi.org/10.3847/1538-4357/ab43e3)
- Astropy Collaboration, Robitaille, T. P., Tollerud, E. J., et al. 2013, *A&A*, 558, A33, doi: [10.1051/0004-6361/201322068](https://doi.org/10.1051/0004-6361/201322068)
- Astropy Collaboration, Price-Whelan, A. M., Sipőcz, B. M., et al. 2018, *AJ*, 156, 123, doi: [10.3847/1538-3881/aabc4f](https://doi.org/10.3847/1538-3881/aabc4f)
- Bacon, R., Vernet, J., Borisova, E., et al. 2014, *The Messenger*, 157, 13
- Benetti, S., Pastorello, A., Elias-Rosa, N., et al. 2014, *The Astronomer's Telegram*, 6185, 1
- Benetti, S., Tomasella, L., Cappellaro, E., et al. 2015, *The Astronomer's Telegram*, 7712, 1
- Bersier, D. 2016, *Transient Name Server Classification Report*, 2016-908, 1
- Bersier, D., Smartt, S., & Yaron, O. 2016, *Transient Name Server Classification Report*, 2016-650, 1
- Bertin, E. 2010, *SWarp: Resampling and Co-adding FITS Images Together*, *Astrophysics Source Code Library*, record ascl:1010.068
- Bertin, E., & Arnouts, S. 1996, *A&AS*, 117, 393, doi: [10.1051/aas:1996164](https://doi.org/10.1051/aas:1996164)
- Bradley, L., Sipőcz, B., Robitaille, T., et al. 2023, *astropy/photutils: 1.8.0*, 1.8.0, Zenodo, doi: [10.5281/zenodo.7946442](https://doi.org/10.5281/zenodo.7946442)
- Bundy, K., Bershady, M. A., Law, D. R., et al. 2015, *ApJ*, 798, 7, doi: [10.1088/0004-637X/798/1/7](https://doi.org/10.1088/0004-637X/798/1/7)
- Cao, Y., Kasliwal, M., AlSayyad, Y., & Kulkarni, S. R. 2014, *The Astronomer's Telegram*, 6826, 1
- Cartier, R., Dennihy, E., Pastorello, A., et al. 2018, *The Astronomer's Telegram*, 11585, 1
- Chen, T.-W., Schady, P., Xiao, L., et al. 2017, *ApJL*, 849, L4, doi: [10.3847/2041-8213/aa8f40](https://doi.org/10.3847/2041-8213/aa8f40)
- Chugai, N. N., & Chevalier, R. A. 2006, *ApJ*, 641, 1051, doi: [10.1086/500539](https://doi.org/10.1086/500539)

**Table 3.** The mid-IR photometry and SED fitting results.

Name	MJD	Epoch	$f_{3.4\mu\text{m}}$	$f_{4.6\mu\text{m}}$	$R_{\text{BB}}$	$M_{\text{dust}}$	$T_{\text{dust}}$	$L_{\text{dust}}$
		days	$\mu\text{Jy}$	$\mu\text{Jy}$	$10^{16}\text{cm}$	$10^{-5}M_{\odot}$	K	$10^6L_{\odot}$
SN 2003gd*	53211	<b>409</b>	$20 \pm 3$	$71 \pm 14$	0.4	<b>1.1</b>	520	0.1
SN2010dr	55570	<b>220</b>	$319 \pm 14$	$395 \pm 15$	$0.69 \pm 0.08$	<b><math>53.7 \pm 11.2</math></b>	$851 \pm 41$	$19.42 \pm 0.02$
SN 2013ej*	56673	238	$823 \pm 99$	$1525 \pm 98$	1.7	62	490	2.9
	56862	<b>261</b>	$630 \pm 75$	$1201 \pm 55$	1.6	<b>74</b>	465	2.2
	57036	439	$41 \pm 7$	$133 \pm 15$	1.2	64	360	0.4
SN 2014az	56831	<b>54</b>	$203 \pm 8$	$227 \pm 14$	$0.44 \pm 0.07$	<b><math>22.5 \pm 6.4</math></b>	$928 \pm 60$	$10.81 \pm 0.01$
	57011	233	$40 \pm 10$	$63 \pm 14$	$0.39 \pm 0.20$	$16.7 \pm 9.9$	$719 \pm 162$	$3.55 \pm 0.01$
SN 2014ay	56918	137	$110 \pm 7$	$188 \pm 11$	$0.77 \pm 0.12$	$65.6 \pm 19.5$	$679 \pm 37$	$11.73 \pm 0.01$
	57101	<b>319</b>	$< 21$	$69 \pm 9$	$< 1.47$	<b><math>&lt; 232</math></b>	$< 456$	$< 11.61$
ASASSN-14az	56827	30	$612 \pm 7$	$790 \pm 13$	$1.04 \pm 0.04$	$121.6 \pm 9.1$	$824 \pm 13$	$39.72 \pm 0.03$
	57006	<b>208</b>	$45 \pm 8$	$161 \pm 16$	$2.12 \pm 0.67$	<b><math>481.1 \pm 301.6</math></b>	$464 \pm 39$	$25.64 \pm 0.08$
SN 2014cw	57166	<b>267</b>	$38 \pm 10$	$70 \pm 16$	$0.54 \pm 0.28$	<b><math>31.6 \pm 19.7</math></b>	$644 \pm 129$	$4.81 \pm 0.01$
ASASSN-14ma	57198	<b>194</b>	$41 \pm 9$	$60 \pm 15$	$0.35 \pm 0.21$	<b><math>13.5 \pm 15.9</math></b>	$749 \pm 176$	$3.27 \pm 0.01$
ASASSN-15ab	57230	<b>205</b>	$51 \pm 10$	$188 \pm 18$	$2.37 \pm 0.78$	<b><math>604.0 \pm 394.8</math></b>	$459 \pm 41$	$31.27 \pm 0.10$
	57419	394	$34 \pm 9$	$126 \pm 17$	$1.99 \pm 0.92$	$424.4 \pm 391.2$	$456 \pm 57$	$21.31 \pm 0.03$
ASASSN-15jp	57369	<b>206</b>	$59 \pm 9$	$91 \pm 15$	$0.46 \pm 0.19$	<b><math>23.6 \pm 18.5</math></b>	$726 \pm 109$	$5.18 \pm 0.01$
ASASSN-15kj	57378	204	$1220 \pm 12$	$1450 \pm 15$	$1.22 \pm 0.03$	$170.5 \pm 8.5$	$884 \pm 10$	$69.92 \pm 0.05$
	57568	<b>395</b>	$995 \pm 16$	$1370 \pm 13$	$1.51 \pm 0.05$	<b><math>254.7 \pm 15.3</math></b>	$785 \pm 11$	$71.33 \pm 0.06$
	57738	565	$696 \pm 12$	$1020 \pm 16$	$1.45 \pm 0.06$	$232.3 \pm 18.8$	$748 \pm 12$	$56.34 \pm 0.05$
	57934	760	$305 \pm 12$	$528 \pm 15$	$1.33 \pm 0.11$	$193.2 \pm 30.8$	$673 \pm 20$	$33.53 \pm 0.02$
	58099	925	$180 \pm 10$	$327 \pm 16$	$1.13 \pm 0.15$	$138.7 \pm 35.1$	$652 \pm 30$	$21.92 \pm 0.02$
ASASSN-15ln	57389	<b>196</b>	$69 \pm 7$	$91 \pm 14$	$0.37 \pm 0.13$	<b><math>15.2 \pm 10.5</math></b>	$807 \pm 114$	$4.64 \pm 0.01$
ASASSN-15ng	57421	<b>194</b>	$58 \pm 9$	$178 \pm 13$	$1.77 \pm 0.45$	<b><math>337.2 \pm 171.5</math></b>	$498 \pm 37$	$22.63 \pm 0.03$
SN 2015bj	57576	<b>227</b>	$57 \pm 9$	$77 \pm 10$	$0.35 \pm 0.12$	<b><math>13.6 \pm 9.2</math></b>	$795 \pm 117$	$3.96 \pm 0.01$
SN 2016B	57543	152	$459 \pm 9$	$687 \pm 15$	$1.22 \pm 0.07$	$164.4 \pm 17.4$	$739 \pm 15$	$38.23 \pm 0.04$
	57742	<b>351</b>	$36 \pm 10$	$137 \pm 21$	$2.12 \pm 1.04$	<b><math>481.4 \pm 472.0</math></b>	$453 \pm 59$	$23.74 \pm 0.03$
SN 2016C	57578	<b>187</b>	$63 \pm 10$	$119 \pm 19$	$0.72 \pm 0.29$	<b><math>55.8 \pm 44.3</math></b>	$639 \pm 87$	$8.24 \pm 0.01$
SN 2016X	57560	152	$513 \pm 8$	$487 \pm 14$	$0.48 \pm 0.04$	$28.5 \pm 3.9$	$1092 \pm 40$	$24.18 \pm 0.01$
	57756	349	$142 \pm 10$	$230 \pm 17$	$0.79 \pm 0.15$	$69.3 \pm 25.4$	$702 \pm 48$	$13.72 \pm 0.01$
	57920	<b>513</b>	$43 \pm 7$	$169 \pm 15$	$2.48 \pm 0.73$	<b><math>661.7 \pm 390.4</math></b>	$446 \pm 35$	$30.81 \pm 0.04$
SN 2016aqf	57646	<b>202</b>	$101 \pm 4$	$113 \pm 8$	$0.31 \pm 0.05$	<b><math>11.1 \pm 3.7</math></b>	$929 \pm 71$	$5.38 \pm 0.01$
SN 2016bkv	57708	239	$221 \pm 13$	$218 \pm 19$	$0.35 \pm 0.08$	$14.5 \pm 6.0$	$1047 \pm 113$	$10.52 \pm 0.01$
	57866	397	$321 \pm 13$	$329 \pm 24$	$0.46 \pm 0.08$	$25.0 \pm 8.4$	$1005 \pm 83$	$15.71 \pm 0.01$
	58070	<b>601</b>	$133 \pm 16$	$186 \pm 20$	$0.57 \pm 0.16$	<b><math>36.6 \pm 20.2</math></b>	$775 \pm 89$	$9.84 \pm 0.01$
SN 2016blz	57599	<b>111</b>	$162 \pm 7$	$303 \pm 12$	$1.12 \pm 0.11$	<b><math>138 \pm 26.5</math></b>	$643 \pm 22$	$20.82 \pm 0.01$
	57798	309	$102 \pm 7$	$149 \pm 12$	$0.54 \pm 0.10$	$32.8 \pm 9.9$	$754 \pm 54$	$8.09 \pm 0.008$
SN 2016bmi	57647	<b>154</b>	$217 \pm 9$	$384 \pm 16$	$1.17 \pm 0.12$	<b><math>150.0 \pm 30.1</math></b>	$663 \pm 24$	$24.92 \pm 0.03$
	57839	347	$67 \pm 8$	$120 \pm 13$	$0.67 \pm 0.19$	$49.6 \pm 27$	$655 \pm 63$	$7.94 \pm 0.01$
SN 2016cdd	57580	<b>58</b>	$267 \pm 7$	$342 \pm 13$	$0.68 \pm 0.06$	<b><math>51.4 \pm 9.0</math></b>	$829 \pm 31$	$17.13 \pm 0.01$
	57775	253	$76 \pm 8$	$120 \pm 13$	$0.58 \pm 0.15$	$34.2 \pm 17.6$	$710 \pm 69$	$7.02 \pm 0.01$
	57942	420	$23 \pm 7$	$55 \pm 13$	$0.71 \pm 0.46$	$54 \pm 47.6$	$556 \pm 113$	$5.17 \pm 0.01$
SN 2016cvk	57887	<b>335</b>	$31 \pm 10$	$61 \pm 16$	$0.54 \pm 0.33$	<b><math>31.8 \pm 32.2</math></b>	$626 \pm 144$	$4.41 \pm 0.01$
SN 2016cyx	57768	<b>192</b>	$81 \pm 12$	$116 \pm 15$	$0.47 \pm 0.16$	<b><math>24.6 \pm 16.7</math></b>	$762 \pm 106$	$6.26 \pm 0.01$
SN 2016gkg	57740	89	$173 \pm 10$	$302 \pm 15$	$1.02 \pm 0.14$	$114.7 \pm 29.7$	$667 \pm 32$	$19.4 \pm 0.01$
	57935	284	$178 \pm 8$	$264 \pm 13$	$0.75 \pm 0.09$	$61.5 \pm 14.9$	$744 \pm 35$	$14.61 \pm 0.01$
	58101	449	$145 \pm 10$	$267 \pm 16$	$1.03 \pm 0.16$	$116.3 \pm 35.7$	$648 \pm 35$	$18.12 \pm 0.01$
	58302	650	$98 \pm 8$	$242 \pm 18$	$1.52 \pm 0.28$	$251.1 \pm 90.2$	$550 \pm 30$	$23.35 \pm 0.07$
	58464	<b>813</b>	$38 \pm 9$	$124 \pm 19$	$1.64 \pm 0.75$	<b><math>290.0 \pm 262.4</math></b>	$482 \pm 60$	$17.54 \pm 0.02$
	58667	1016	$44 \pm 8$	$114 \pm 16$	$1.1 \pm 0.42$	$131.4 \pm 100.3$	$540 \pm 63$	$11.51 \pm 0.01$
	58828	1177	$21 \pm 7$	$38 \pm 12$	$0.37 \pm 0.29$	$15.2 \pm 23.6$	$658 \pm 180$	$2.48 \pm 0.01$

Table 3. Continued

Name	MJD	Epoch	$f_{3.4\mu\text{m}}$	$f_{4.6\mu\text{m}}$	R <sub>BB</sub>	M <sub>dust</sub>	T <sub>dust</sub>	L <sub>dust</sub>
		days	$\mu\text{Jy}$	$\mu\text{Jy}$	$10^{16}\text{cm}$	$10^{-5}M_{\odot}$	K	$10^6L_{\odot}$
SN 2016hgm	57947	<b>267</b>	47 ± 11	111 ± 20	0.96 ± 0.47	<b>98.5 ± 96.5</b>	566 ± 88	9.98 ± 0.01
SN 2016hwn	57902	<b>203</b>	54 ± 8	102 ± 14	0.66 ± 0.23	<b>47.5 ± 33.1</b>	639 ± 77	7.04 ± 0.01
SN 2016iae	57783	<b>84</b>	285 ± 21	578 ± 27	1.76 ± 0.25	<b>336.2 ± 93.9</b>	612 ± 30	43.5 ± 0.02
SN 2017bzb	58061	<b>242</b>	247 ± 7	653 ± 14	2.75 ± 0.15	<b>813.3 ± 90.4</b>	533 ± 9	68.2 ± 0.09
SN 2017faa	58128	197	294 ± 10	359 ± 17	0.64 ± 0.07	46.6 ± 9.93	861 ± 40	17.53 ± 0.01
	58287	<b>355</b>	355 ± 12	422 ± 13	0.66 ± 0.06	<b>50.2 ± 8.24</b>	882 ± 34	20.44 ± 0.02
	58493	562	123 ± 13	177 ± 18	0.59 ± 0.16	38.5 ± 19.6	757 ± 79	9.64 ± 0.01
	58654	723	60 ± 9	91 ± 14	0.46 ± 0.18	22.9 ± 17.7	731 ± 110	5.14 ± 0.01
SN 2017fbu	58124	<b>187</b>	47 ± 9	74 ± 15	0.42 ± 0.21	<b>19.7 ± 9.3</b>	720 ± 138	4.23 ± 0.01
SN 2017ffq	58195	251	102 ± 11	88 ± 13	0.17 ± 0.07	3.7 ± 2.8	1223 ± 276	4.76 ± 0.01
	58359	<b>415</b>	6 ± 2	11 ± 3	0.20 ± 0.15	<b>4.4 ± 6.7</b>	662 ± 179	0.73 ± 0.01
SN 2017fqk	58132	<b>173</b>	39 ± 11	55 ± 19	0.32 ± 0.24	<b>11.3 ± 10.3</b>	768 ± 242	2.95 ± 0.01
SN 2017gax	58124	<b>145</b>	143 ± 10	264 ± 10	1.03 ± 0.13	<b>117 ± 28.8</b>	646 ± 30	17.91 ± 0.01
	58327	347	34 ± 11	56 ± 11	0.40 ± 0.25	17.9 ± 21.7	692 ± 166	3.39 ± 0.01
SN 2017gmr	58124	<b>124</b>	1300 ± 13	1790 ± 15	1.74 ± 0.04	<b>336.8 ± 15.1</b>	783 ± 8	93.54 ± 0.08
	58324	324	134 ± 11	244 ± 15	0.98 ± 0.17	103.9 ± 35.4	652 ± 41	16.37 ± 0.02
	58485	484	< 39	89 ± 16	< 0.84	< 77.1	< 568	< 7.89
SN 2017hcc	58287	259	764 ± 10	1060 ± 21	1.36 ± 0.06	207.0 ± 18.3	777 ± 14	56.13 ± 0.05
	58450	421	1550 ± 11	1480 ± 17	0.85 ± 0.03	87.2 ± 4.7	1088 ± 16	72.62 ± 0.04
	58651	623	1070 ± 12	1290 ± 14	1.18 ± 0.04	159.6 ± 9.2	872 ± 12	62.63 ± 0.05
	58814	785	800 ± 8	1080 ± 15	1.3 ± 0.04	190.6 ± 11.7	796 ± 10	55.72 ± 0.05
	59019	<b>990</b>	413 ± 9	733 ± 18	1.63 ± 0.10	<b>289.3 ± 33.3</b>	662 ± 13	47.74 ± 0.05
	59179	1151	323 ± 7	605 ± 13	1.6 ± 0.08	279.8 ± 29.2	641 ± 11	41.72 ± 0.02
	59383	1354	180 ± 8	355 ± 20	1.32 ± 0.175	189.4 ± 49.7	622 ± 27	25.83 ± 0.01
SN 2017hpi	58221	169	221 ± 9	433 ± 15	1.45 ± 0.13	227.8 ± 40.4	624 ± 19	31.41 ± 0.02
	58431	<b>378</b>	43 ± 7	144 ± 13	1.82 ± 0.55	<b>355.2 ± 213.4</b>	477 ± 40	20.84 ± 0.02
SN 2017ivv	58240	<b>141</b>	141 ± 7	439 ± 16	2.85 ± 0.28	<b>871.2 ± 171.8</b>	494 ± 14	57.12 ± 0.06
	58404	305	31 ± 6	61 ± 12	0.51 ± 0.25	32.8 ± 23.3	622 ± 97	4.46 ± 0.01
SN 2018pq	58304	<b>147</b>	63 ± 9	239 ± 12	2.82 ± 0.67	<b>852.8 ± 402.2</b>	452 ± 30	41.65 ± 0.05
SN 2018bbl	58423	<b>202</b>	< 24	125 ± 14	< 4.23	< <b>1919.5</b>	< 373	< 47.34
SN 2018cuf	58594	<b>301</b>	< 18	72 ± 14	< 2.21	< <b>522.8</b>	< 410	< 18.11
SN 2020tlf	59382	273	29 ± 7	42 ± 12	0.29 ± 0.20	9.0 ± 12.2	758 ± 203	2.26 ± 0.01
	59587	<b>479</b>	37 ± 9	52 ± 11	0.30 ± 0.17	<b>10.0 ± 11.2</b>	779 ± 182	2.72 ± 0.01

NOTE—The data at the epoch in bold is used as the dust contribution of each SN in Figure 12. The dust type is classified into pre-exiting (pre) and newly-formed (nf) dust. \*The photometry of SN 2003gd and SN 2013ej are from *Spitzer* at 3.5 $\mu\text{m}$  and 4.5 $\mu\text{m}$ , and the corresponding dust parameters are directly from Szalai et al. (2019).

(This table is available in machine-readable form.)

- Dimitriadis, G., Pursiainen, M., Smith, M., et al. 2016, *The Astronomer's Telegram*, 9660, 1
- Domínguez, A., Siana, B., Henry, A. L., et al. 2013, *ApJ*, 763, 145, doi: [10.1088/0004-637X/763/2/145](https://doi.org/10.1088/0004-637X/763/2/145)
- Dong, S., Bersier, D., & Prieto, J. L. 2017, *Transient Name Server Classification Report*, 2017-1103, 1
- Dopita, M. A., Kewley, L. J., Sutherland, R. S., & Nicholls, D. C. 2016, *Ap&SS*, 361, 61, doi: [10.1007/s10509-016-2657-8](https://doi.org/10.1007/s10509-016-2657-8)
- Dubey, M., Misra, K., Dastidar, R., et al. 2025, *MNRAS*, 541, 384, doi: [10.1093/mnras/staf1014](https://doi.org/10.1093/mnras/staf1014)
- Eldridge, J. J., Stanway, E. R., Xiao, L., et al. 2017, *PASA*, 34, e058, doi: [10.1017/pasa.2017.51](https://doi.org/10.1017/pasa.2017.51)
- Elias-Rosa, N., Tartaglia, L., Cappellaro, E., et al. 2014, *The Astronomer's Telegram*, 6440, 1
- Falco, E., Calkins, M., Challis, P., et al. 2016, *The Astronomer's Telegram*, 9237, 1
- Falco, E., Irwin, J., Challis, P., et al. 2015, *The Astronomer's Telegram*, 7557, 1
- Fazio, G. G., Hora, J. L., Allen, L. E., et al. 2004, *ApJS*, 154, 10, doi: [10.1086/422843](https://doi.org/10.1086/422843)
- Ferland, G. J., Porter, R. L., van Hoof, P. A. M., et al. 2013, *RMxAA*, 49, 137. <https://arxiv.org/abs/1302.4485>
- Fox, O. D., Chevalier, R. A., Dwek, E., et al. 2010, *ApJ*, 725, 1768, doi: [10.1088/0004-637X/725/2/1768](https://doi.org/10.1088/0004-637X/725/2/1768)
- Fox, O. D., Filippenko, A. V., Skrutskie, M. F., et al. 2013, *AJ*, 146, 2, doi: [10.1088/0004-6256/146/1/2](https://doi.org/10.1088/0004-6256/146/1/2)
- Fox, O. D., Chevalier, R. A., Skrutskie, M. F., et al. 2011, *ApJ*, 741, 7, doi: [10.1088/0004-637X/741/1/7](https://doi.org/10.1088/0004-637X/741/1/7)
- Fox, O. D., Smith, N., Ammons, S. M., et al. 2015, *MNRAS*, 454, 4366, doi: [10.1093/mnras/stv2270](https://doi.org/10.1093/mnras/stv2270)
- Fox, O. D., Johansson, J., Kasliwal, M., et al. 2016, *ApJL*, 816, L13, doi: [10.3847/2041-8205/816/1/L13](https://doi.org/10.3847/2041-8205/816/1/L13)
- Fransson, C., Ergon, M., Challis, P. J., et al. 2014, *ApJ*, 797, 118, doi: [10.1088/0004-637X/797/2/118](https://doi.org/10.1088/0004-637X/797/2/118)
- Galbany, L., Gonzalez-Gaitan, S., Dong, S., Chen, P., & Hamuy, M. 2016a, *The Astronomer's Telegram*, 8541, 1
- Galbany, L., Anderson, J. P., Rosales-Ortega, F. F., et al. 2016b, *MNRAS*, 455, 4087, doi: [10.1093/mnras/stv2620](https://doi.org/10.1093/mnras/stv2620)
- Galbany, L., Anderson, J. P., Sánchez, S. F., et al. 2018, *ApJ*, 855, 107, doi: [10.3847/1538-4357/aaaf20](https://doi.org/10.3847/1538-4357/aaaf20)
- Gall, C., Hjorth, J., & Andersen, A. C. 2011, *A&A Rv*, 19, 43, doi: [10.1007/s00159-011-0043-7](https://doi.org/10.1007/s00159-011-0043-7)
- Graham, M. L., Harris, C. E., Fox, O. D., et al. 2017, *ApJ*, 843, 102, doi: [10.3847/1538-4357/aa78ee](https://doi.org/10.3847/1538-4357/aa78ee)
- Gutiérrez, C. P., Pastorello, A., Jerkstrand, A., et al. 2020, *MNRAS*, 499, 974, doi: [10.1093/mnras/staa2763](https://doi.org/10.1093/mnras/staa2763)
- Holoien, T. W.-S., Shappee, B. J., Brimacombe, J., et al. 2014, *The Astronomer's Telegram*, 6126, 1
- Hosseinizadeh, G., Arcavi, I., Howell, D. A., McCully, C., & Valenti, S. 2016, *The Astronomer's Telegram*, 9065, 1
- Hosseinizadeh, G., Valenti, S., McCully, C., et al. 2018, *ApJ*, 861, 63, doi: [10.3847/1538-4357/aac5f6](https://doi.org/10.3847/1538-4357/aac5f6)
- Hu, L., Wang, L., & Chen, X. 2021, *sfft*, 1.0.3, Zenodo, doi: [10.5281/zenodo.5521634](https://doi.org/10.5281/zenodo.5521634)
- Hu, L., Wang, L., Chen, X., & Yang, J. 2022, *ApJ*, 936, 157, doi: [10.3847/1538-4357/ac7394](https://doi.org/10.3847/1538-4357/ac7394)
- Jacobson-Galán, W. V., Dessart, L., Jones, D. O., et al. 2022, *ApJ*, 924, 15, doi: [10.3847/1538-4357/ac3f3a](https://doi.org/10.3847/1538-4357/ac3f3a)
- Jha, S. W., Camacho, Y., Dettman, K., et al. 2017, *The Astronomer's Telegram*, 10640, 1
- Jha, S. W., Foley, R. J., & Skelton, R. 2016, *The Astronomer's Telegram*, 9754, 1
- Jha, S. W., Camacho, Y., Dai, M., et al. 2018, *The Astronomer's Telegram*, 11777, 1
- Jones, C. S. 2001, *Journal of Financial Economics*, 62, 293, doi: [https://doi.org/10.1016/S0304-405X\(01\)00079-4](https://doi.org/10.1016/S0304-405X(01)00079-4)
- Kasliwal, M. M., Bally, J., Masci, F., et al. 2017, *ApJ*, 839, 88, doi: [10.3847/1538-4357/aa6978](https://doi.org/10.3847/1538-4357/aa6978)
- Kinugasa, K., & Takahashi, H. 2010, *Central Bureau Electronic Telegrams*, 2328, 2
- Kozasa, T., Nozawa, T., Tominaga, N., et al. 2009, in *Astronomical Society of the Pacific Conference Series*, Vol. 414, *Cosmic Dust - Near and Far*, ed. T. Henning, E. Grün, & J. Steinacker, 43, doi: [10.48550/arXiv.0903.0217](https://doi.org/10.48550/arXiv.0903.0217)
- Kuncarayakti, H., Anderson, J. P., Galbany, L., et al. 2018, *A&A*, 613, A35, doi: [10.1051/0004-6361/201731923](https://doi.org/10.1051/0004-6361/201731923)
- Lang, D. 2014, *AJ*, 147, 108, doi: [10.1088/0004-6256/147/5/108](https://doi.org/10.1088/0004-6256/147/5/108)
- Magee, M., Bar, I., Johansson, J., et al. 2016a, *The Astronomer's Telegram*, 8935, 1
- Magee, M., Bar, I., Leloudas, G., et al. 2016b, *The Astronomer's Telegram*, 8963, 1
- Margutti, R., Kamble, A., Milisavljevic, D., et al. 2017, *ApJ*, 835, 140, doi: [10.3847/1538-4357/835/2/140](https://doi.org/10.3847/1538-4357/835/2/140)
- Mast, D., Rosales-Ortega, F. F., Sánchez, S. F., et al. 2014, *A&A*, 561, A129, doi: [10.1051/0004-6361/201321789](https://doi.org/10.1051/0004-6361/201321789)
- Matsuura, M., Barlow, M. J., Zijlstra, A. A., et al. 2009, *MNRAS*, 396, 918, doi: [10.1111/j.1365-2966.2009.14743.x](https://doi.org/10.1111/j.1365-2966.2009.14743.x)
- Mauerhan, J. C., Filippenko, A. V., Zheng, W., et al. 2018, *MNRAS*, 478, 5050, doi: [10.1093/mnras/sty1307](https://doi.org/10.1093/mnras/sty1307)
- Meikle, W. P. S., Kotak, R., Farrah, D., et al. 2011, *ApJ*, 732, 109, doi: [10.1088/0004-637X/732/2/109](https://doi.org/10.1088/0004-637X/732/2/109)
- Meisner, A. M., Lang, D., & Schlegel, D. J. 2017a, *AJ*, 153, 38, doi: [10.3847/1538-3881/153/1/38](https://doi.org/10.3847/1538-3881/153/1/38)
- . 2017b, *AJ*, 154, 161, doi: [10.3847/1538-3881/aa894e](https://doi.org/10.3847/1538-3881/aa894e)
- Milisavljevic, D., Margutti, R., Kamble, A., et al. 2015, *ApJ*, 815, 120, doi: [10.1088/0004-637X/815/2/120](https://doi.org/10.1088/0004-637X/815/2/120)

- Moriya, T. J., Galbany, L., Jiménez-Palau, C., et al. 2023, *A&A*, 677, A20, doi: [10.1051/0004-6361/202346703](https://doi.org/10.1051/0004-6361/202346703)
- Morrell, N., Shappee, B., Drout, M., & Dong, S. 2017, *The Astronomer's Telegram*, 10240, 1
- Myers, C., De, K., Yan, L., et al. 2024, *ApJ*, 976, 230, doi: [10.3847/1538-4357/ad8922](https://doi.org/10.3847/1538-4357/ad8922)
- O'Neill, D., Magee, M., Anderson, J., et al. 2017, *The Astronomer's Telegram*, 10909, 1
- Parker, S., Yusa, T., Shima, K., et al. 2014, *Central Bureau Electronic Telegrams*, 3872, 1
- Pessi, T., Anderson, J. P., Lyman, J. D., et al. 2023b, *ApJL*, 955, L29, doi: [10.3847/2041-8213/acf7c6](https://doi.org/10.3847/2041-8213/acf7c6)
- Pessi, T., Prieto, J. L., Anderson, J. P., et al. 2023a, *A&A*, 677, A28, doi: [10.1051/0004-6361/202346512](https://doi.org/10.1051/0004-6361/202346512)
- Piascik, A. S., & Steele, I. A. 2016, *The Astronomer's Telegram*, 8505, 1
- Rodriguez, O., & Prieto, J. L. 2017a, *The Astronomer's Telegram*, 10580, 1
- . 2017b, *The Astronomer's Telegram*, 10586, 1
- Ryder, S. D., Kool, E. C., Stockdale, C. J., Romero-Canizales, C., & Kotak, R. 2016, *The Astronomer's Telegram*, 8815, 1
- Sahu, D. K., Anupama, G. C., Srivastav, S., & Chakradhari, N. K. 2016, *The Astronomer's Telegram*, 8514, 1
- Salvatier J., Wiecki TV, F. C. 2016, *PeerJ Computer Science*, 2:e55, doi: <https://doi.org/10.7717/peerj-cs.55>
- Sarangi, A. 2022, *A&A*, 668, A57, doi: [10.1051/0004-6361/202244391](https://doi.org/10.1051/0004-6361/202244391)
- Shahbandeh, M., Sarangi, A., Temim, T., et al. 2023, *MNRAS*, 523, 6048, doi: [10.1093/mnras/stad1681](https://doi.org/10.1093/mnras/stad1681)
- Shappee, B. J., & Morrell, N. 2015, *The Astronomer's Telegram*, 7692, 1
- Shappee, B. J., Prieto, J. L., Seibert, M., & Johnston, E. 2015b, *The Astronomer's Telegram*, 8031, 1
- Shappee, B. J., Prieto, J. L., Holoiën, T. W.-S., et al. 2015a, *The Astronomer's Telegram*, 6882, 1
- Siebert, M. R., Kwok, L. A., Johansson, J., et al. 2024, *ApJ*, 960, 88, doi: [10.3847/1538-4357/ad0975](https://doi.org/10.3847/1538-4357/ad0975)
- Silverman, J. M., Nugent, P. E., Gal-Yam, A., et al. 2013, *ApJ*, 772, 125, doi: [10.1088/0004-637X/772/2/125](https://doi.org/10.1088/0004-637X/772/2/125)
- Smartt, S. J. 2009, *ARA&A*, 47, 63, doi: [10.1146/annurev-astro-082708-101737](https://doi.org/10.1146/annurev-astro-082708-101737)
- . 2015, *PASA*, 32, e016, doi: [10.1017/pasa.2015.17](https://doi.org/10.1017/pasa.2015.17)
- Smith, N. 2017, *Interacting Supernovae: Types IIIn and Ibn*, In "Handbook of Supernovae", edited by Athem W. Alsabti and Paul Murdin, doi: [10.1007/978-3-319-21846-5\\_38](https://doi.org/10.1007/978-3-319-21846-5_38)
- Somero, A., Kuncarayakti, H., Mattila, S., et al. 2017, *The Astronomer's Telegram*, 10594, 1
- Sun, L., Xiao, L., & Li, G. 2022, *MNRAS*, 513, 4057, doi: [10.1093/mnras/stac1121](https://doi.org/10.1093/mnras/stac1121)
- Sun, N.-C., Maund, J. R., Crowther, P. A., Fang, X., & Zapartas, E. 2021, *MNRAS*, 504, 2253, doi: [10.1093/mnras/stab994](https://doi.org/10.1093/mnras/stab994)
- Szalai, T., & Vinkó, J. 2013, *A&A*, 549, A79, doi: [10.1051/0004-6361/201220015](https://doi.org/10.1051/0004-6361/201220015)
- Szalai, T., Vinkó, J., Balog, Z., et al. 2011, *A&A*, 527, A61, doi: [10.1051/0004-6361/201015624](https://doi.org/10.1051/0004-6361/201015624)
- Szalai, T., Zsíros, S., Fox, O. D., Pejcha, O., & Müller, T. 2019, *ApJS*, 241, 38, doi: [10.3847/1538-4365/ab10df](https://doi.org/10.3847/1538-4365/ab10df)
- Szalai, T., Fox, O. D., Arendt, R. G., et al. 2021, *ApJ*, 919, 17, doi: [10.3847/1538-4357/ac0e2b](https://doi.org/10.3847/1538-4357/ac0e2b)
- Szalai, T., Zsíros, S., Jencson, J., et al. 2025, *A&A*, 697, A132, doi: [10.1051/0004-6361/202451470](https://doi.org/10.1051/0004-6361/202451470)
- Tartaglia, L., Valenti, S., Bostroem, K. A., Yang, S., & Hosseinzadeh, G. 2017, *The Astronomer's Telegram*, 10603, 1
- Tinyanont, S., Kasliwal, M. M., Fox, O. D., et al. 2016, *ApJ*, 833, 231, doi: [10.3847/1538-4357/833/2/231](https://doi.org/10.3847/1538-4357/833/2/231)
- Tinyanont, S., Lau, R. M., Kasliwal, M. M., et al. 2019, *ApJ*, 887, 75, doi: [10.3847/1538-4357/ab521b](https://doi.org/10.3847/1538-4357/ab521b)
- Valenti, S., Sand, D., Pastorello, A., et al. 2014, *MNRAS*, 438, L101, doi: [10.1093/mnras/slt171](https://doi.org/10.1093/mnras/slt171)
- Van Dyk, S. D., Li, W., & Filippenko, A. V. 2003, *PASP*, 115, 1289, doi: [10.1086/378308](https://doi.org/10.1086/378308)
- Van Dyk, S. D., Zheng, W., Shivvers, I., et al. 2016, *The Astronomer's Telegram*, 9573, 1
- Verheijen, M. A. W., Bershady, M. A., Andersen, D. R., et al. 2004, *Astronomische Nachrichten*, 325, 151, doi: [10.1002/asna.200310197](https://doi.org/10.1002/asna.200310197)
- Virtanen, P., Gommers, R., Oliphant, T. E., et al. 2020, *Nature Methods*, 17, 261, doi: [10.1038/s41592-019-0686-2](https://doi.org/10.1038/s41592-019-0686-2)
- Wang, L., Hu, M., Wang, L., et al. 2024, *Nature Astronomy*, 8, 504, doi: [10.1038/s41550-024-02197-9](https://doi.org/10.1038/s41550-024-02197-9)
- Waskom, M. L. 2021, *Journal of Open Source Software*, 6, 3021, doi: [10.21105/joss.03021](https://doi.org/10.21105/joss.03021)
- Wright, E. L., Eisenhardt, P. R. M., Mainzer, A. K., et al. 2010, *AJ*, 140, 1868, doi: [10.1088/0004-6256/140/6/1868](https://doi.org/10.1088/0004-6256/140/6/1868)
- Xi, Q., Sun, N.-C., Zhao, Y.-H., et al. 2025, *MNRAS*, 542, 1852, doi: [10.1093/mnras/staf1275](https://doi.org/10.1093/mnras/staf1275)
- Xiao, L., Galbany, L., Eldridge, J. J., & Stanway, E. R. 2019, *MNRAS*, 482, 384, doi: [10.1093/mnras/sty2557](https://doi.org/10.1093/mnras/sty2557)
- Zheng, X.-M., & Zhang, J.-J. 2016, *The Astronomer's Telegram*, 8584, 1
- Zsíros, S., Szalai, T., De Looze, I., et al. 2023, *arXiv e-prints*, arXiv:2310.03448, doi: [10.48550/arXiv.2310.03448](https://doi.org/10.48550/arXiv.2310.03448)
- . 2024, *MNRAS*, 529, 155, doi: [10.1093/mnras/stae507](https://doi.org/10.1093/mnras/stae507)